



# A Comparative Simulation Study of Hot and Ultra-hot Jupiter Atmospheres using Different Ground-based High-resolution Spectrographs with Cross-correlation Spectroscopy

DWAIPAYAN DUBEY <sup>1,2,3,4</sup> AND LITON MAJUMDAR <sup>1,2</sup>

<sup>1</sup>*School of Earth and Planetary Sciences, National Institute of Science Education and Research, Jatni 752050, Odisha, India*

<sup>2</sup>*Homi Bhabha National Institute, Training School Complex, Anushaktinagar, Mumbai 400094, India*

<sup>3</sup>*Universitäts-Sternwarte, Fakultät für Physik, Ludwig-Maximilians-Universität München, Scheinerstr. 1, D-81679 München, Germany*

<sup>4</sup>*Exzellenzcluster 'Origins', Boltzmannstr. 2, D-85748 Garching, Germany*

## ABSTRACT

In the era of state-of-the-art space-borne telescopes, high-resolution ground-based observation has emerged as a crucial method for characterizing exoplanets, providing essential insights into their atmospheric compositions. In the optical and NIR regions, high-resolution spectroscopy has been powerful for hot Jupiters (HJ) and ultra-hot Jupiters (UHJ) during their primary transits, as it can probe molecules with better sensitivity. Here, we focus on a comparative simulation study of WASP-76 b (UHJ) and WASP-77 A b (HJ) for different number of transits, utilizing three ground-based spectrographs (GIANO-B (TNG), CARMENES (CAHA), and ANDES (E-ELT)) with varying instrumental parameters, spectral coverages, and resolutions. We aim to evaluate the feasibility of the upcoming ground-based European Extremely Large Telescope (E-ELT) in probing molecules from planet atmospheres and how it surpasses other ground-based observatories in terms of detectability. With the 1-D model, petitCODE, we have self-consistently simulated the atmospheric pressure-temperature profiles, which are subsequently integrated into the 1-D chemical kinetics model, VULCAN, to evolve the atmospheric chemistry. High-resolution spectra are obtained by performing line-by-line radiative transfer using petitRADTRANS. Finally, we use the resulting spectra to assess the detectability ( $\sigma_{\text{det}}$ ) of molecular bands, employing the ground-based noise simulator SPECTR. Utilizing cross-correlation spectroscopy, we have successfully demonstrated the robust consistency between our simulation study and real-time observations for both planets. ANDES excels overall in molecular detection due to its enhanced instrumental architecture, reinforcing E-ELT's importance for studying exoplanet atmospheres. Additionally, our theoretical simulations predict the detection of CO, NH<sub>3</sub>, and H<sub>2</sub>S on WASP-76 b atmosphere with a  $\sigma_{\text{det}} > 3$ .

**Keywords:** Extrasolar gaseous planets (2172); Hot Jupiters (753); Exoplanet atmospheres (487); Exoplanet atmospheric composition (2021); Spectroscopy (1558); High resolution spectroscopy (2096)

## 1. INTRODUCTION

Exoplanetary science has made remarkable advancements in recent years, driven by numerous discoveries that have significantly changed our understanding of planetary systems and their complex characteristics. In recent decades, spectroscopic measurements have become an essential window for understanding atmospheric compositions, its dynamics, and temperature profiles of exoplanets (Crossfield 2015). While space-based observations have historically been crucial in providing initial characterizations of atmospheres for transit-

ing exoplanets, ground-based observations have increasingly taken on a significant role in undertaking in-depth investigations of their atmospheric chemistry (Snellen et al. 2010; Wyttenbach et al. 2015; Brogi et al. 2016, 2018; Alonso-Floriano et al. 2019; Sánchez-López et al. 2019; Giacobbe et al. 2021). In contrast to low-resolution spectroscopy, high-resolution spectroscopy offers the clear differentiation of molecular fingerprints originating from various species, hence facilitating more accurate detection. The initial breakthrough in ground-based observations occurred with the detection of Na in the atmospheres of HD 189733 b (Redfield et al. 2008) and HD 209458 b (Snellen et al. 2008). Since then, a large number of molecules have been identified in H<sub>2</sub>-dominated atmospheres of gas giants, primarily in the near-infrared spectral range, leveraging high-resolution spec-

troscopy: H<sub>2</sub>O (Birkby et al. 2013a; Alonso-Floriano et al. 2019), CO (Snellen et al. 2010; Brogi et al. 2012), CH<sub>4</sub> (Guilluy et al. 2019), C<sub>2</sub>H<sub>2</sub>, NH<sub>3</sub> (Giacobbe et al. 2021; Carleo et al. 2022), HCN (Hawker et al. 2018; Cabot et al. 2019), etc.

Ground-based observatories, particularly the inbuilt high-resolution spectrographs, can resolve the molecular features into an ensemble of distinctive lines. In spectroscopy, the signal-to-noise ratio improves as the square root of the number of lines observed ( $N_{\text{lines}}$ ) in a planetary spectrum, hence making high-resolution spectroscopy more suitable for broadband absorbers of comparable line strengths (Birkby 2018). For high-resolution spectroscopy, this can be understood from the simplified first-order signal-to-noise ratio equation from Birkby (2018) in the photon-limited region:

$$\text{SNR}_{\text{planet}} = \left( \frac{S_p}{S_*} \right) \text{SNR}_{\text{star}} \sqrt{N_{\text{lines}}}$$

Here,  $\frac{S_p}{S_*}$  is the planet-to-star signal ratio and  $\text{SNR}_{\text{star}}$  is the square root of the photon-limited, total signal-to-noise of the host star. However, this method encounters the inherent challenge of disentangling the planetary signals from strong stellar and telluric backgrounds (Sánchez-López et al. 2019). This challenge can be effectively addressed through the detrending process. It incorporates Doppler shifts into the planet spectra over an extended observation period during the transit and, consequently, separates the planet signal successfully from the complex backgrounds of stellar and telluric lines. The detrended spectra are then subjected to cross-correlation with molecular templates, thereby quantifying the detection significance associated with different molecules (Snellen et al. 2010; Brogi et al. 2012; Birkby et al. 2013b).

The increased spectral resolution is particularly significant when studying the expanded absorption and emission characteristics observed in hot Jupiters (HJs) and ultra-hot Jupiters (UHJs), as they often display pronounced thermal inversions and exhibit unique chemical compositions (Fortney et al. 2008; Madhusudhan & Seager 2010; Line et al. 2016; Parmentier et al. 2018; Arcangeli et al. 2018; Bell & Cowan 2018). These gas giants are of great importance in the realm of exoplanetary science since they can challenge our current understanding of the planetary formation, migration, and atmospheric evolution (Wright et al. 2012; Dash et al. 2022). While HJs are recognized for their elevated temperatures, UHJs, positioned in even closer proximity to their host stars, experience substantial irradiation, which causes them to have a day-side temperature  $\gtrsim 2200$  K (Parmentier et al. 2018). These extreme climatic conditions facilitate the development of unique and often exotic atmospheric chemical processes such as the thermal dissociation of molecules followed by recombination of them on the cooler night side

(Parmentier et al. 2018; Arcangeli et al. 2018; Bell & Cowan 2018). Furthermore, they represent the most extensively observed category of exoplanets to date and, consequently, the most preferred targets for ground-based observations.

WASP-77 A b and WASP-76 b, our targeted HJ and UHJ, are crucial in this regard as they show distinct non-inverted and inverted behaviors, respectively, in the pressure-temperature profile (PT profile) (Edwards et al. 2020; Line et al. 2021; Changeat et al. 2022; Edwards & Changeat 2024) and thus have different implications on their atmospheres. While several atomic and ionic species have been detected in the atmospheres of UHJs (Hoeijmakers et al. 2019, 2020; Casasayas-Barris et al. 2019; Tabernero et al. 2021), it is equally expected to have diatomic and triatomic molecular species as a crucial part of their atmospheric compositions (Landman et al. 2021). The recent detections of OH, H<sub>2</sub>O, and HCN in the atmosphere of WASP-76 b using CAREMENS spectrograph serve as compelling evidence supporting this fact (Sánchez-López et al. 2022; Landman et al. 2021). Conversely, CO and H<sub>2</sub>O line detections on WASP-77 A b using IGRINS spectrometer paves the way for conducting a simultaneous comprehensive analysis to study HJs too using ground-based observation (Line et al. 2021).

In this work, we present a complementary analysis of WASP-77 A b and WASP-76 b atmospheres using three high-resolution ground-based spectrographs: GIANO-B (Telescopio Nazionale Galileo: TNG)<sup>1</sup> (Oliva et al. 2012), CARMENES (Centro Astronomico Hispano Alemán: CAHA)<sup>2</sup> (Quirrenbach et al. 2014, 2018), and ANDES (European Extremely Large Telescope: E-ELT; From this point forward, throughout this paper, the E-ELT will be referred to as the ELT.)<sup>3</sup> (Di Marcantonio et al. 2022). Our main motivation lies in understanding the spectrographs' ability to probe different molecular bands using cross-correlation spectroscopy. In section 2, we have outlined our assumptions and methods for simulating the planet's atmosphere using the 1-D radiative-convective equilibrium model, petitCODE (Mollière et al. 2015; Mollière 2017), and 1-D chemical kinetics model, VULCAN (Tsai et al. 2017, 2021). In addition, we have briefed our method of calculating synthetic observation using the 1-D radiative transfer model, petitRADTRANS (Mollière et al. 2019, 2020), and the ground-based noise simulator, Spectral Planetary ELT Calculator (SPECTR) (Currie et al. 2023). The next section, i.e., Section 3, presents our results from the atmospheric models and the detection significance of molecular bands. Finally, we end up with our findings in Section 4.

<sup>1</sup> <https://www.tng.iac.es/instruments/giano-b/>

<sup>2</sup> <https://www.caha.es/telescope-3-5m/carmenes>

<sup>3</sup> <https://elt.eso.org/instrument/ANDES/>

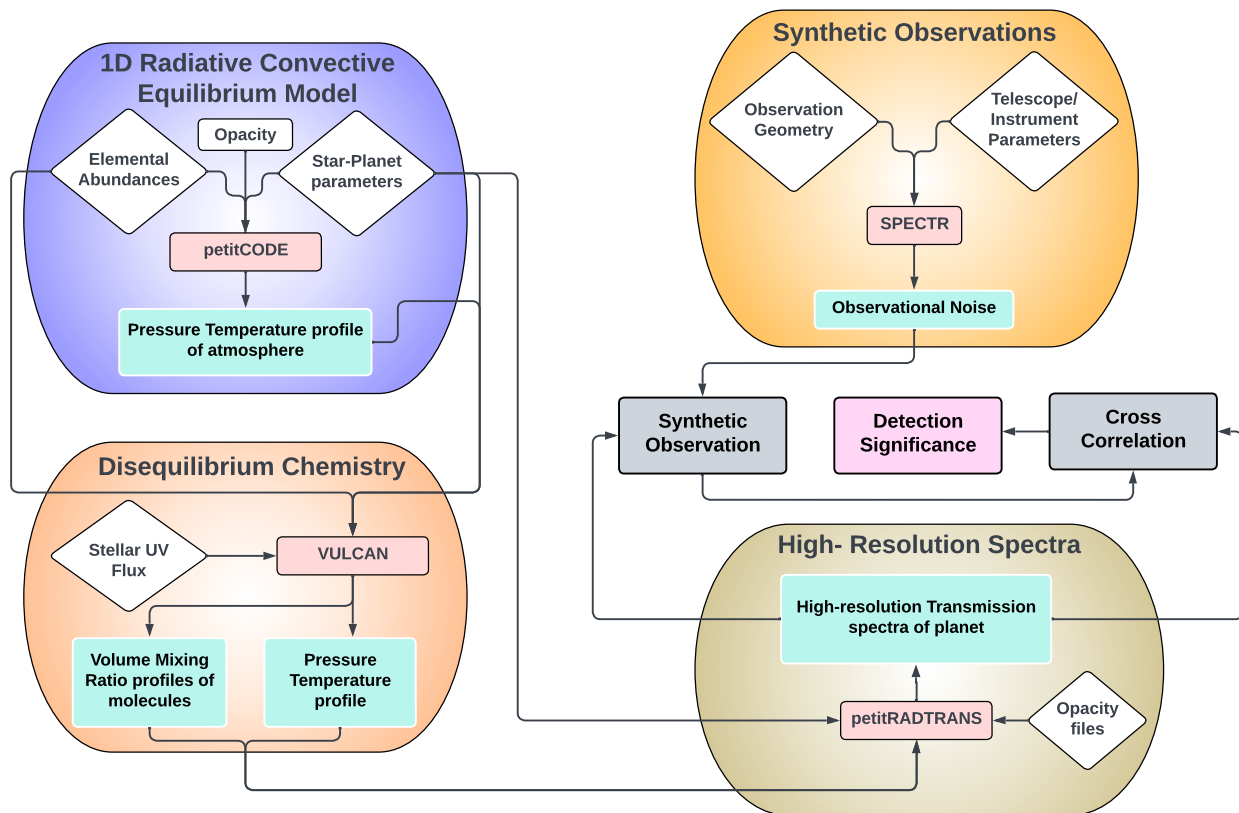


**Figure 1.** Flowchart representing our methodical pipeline: The big boxes represent the four different pillars (radiative-convective equilibrium calculation, disequilibrium chemistry, high-resolution spectra, and synthetic observations), which are connected with each other, of our analysis. The cyan rectangles represent the outputs from each model, while the white shapes are the user-specified inputs for the respective models. Gray rectangles are the outcomes of the whole pipeline, which lead to the calculation of the detection significance of molecular bands.

## 2. METHODS

Our methodical pipeline for assessing the detectability of molecular spectral features using the cross-correlation analysis is outlined in Figure 1. In this current section, we discuss a detailed description of the methods followed.

### 2.1. Atmospheric structures of WASP-76 *b* and WASP-77 *A*

The physical characteristics of a planet’s atmosphere exert a direct influence on its spectral properties and molecular abundance profiles. We self-consistently construct the PT profiles for these two planets using 1-D forward model petitCODE (see Figure 2). petitCODE employs a radiative-convective and thermochemical equilibrium assumption to simulate planetary atmospheres numerically. Based on the input parameters (star and planet parameters for both systems are listed in Table 1), petitCODE iterates the atmospheric structure of the planet till it achieves an equilibrium between the chemical abundances, their opacities and radiation fields with the PT profile of the atmosphere. It solves the radia-

tive transfer using the Feautrier method and implements the Accelerated Lambda Iteration (Olson et al. 1986) and Ng acceleration (Ng 1974) methods to expedite convergence.

We have used petitCODE’s default chemical parameters for the calculation and considered  $\text{CH}_4$ ,  $\text{H}_2\text{O}$ ,  $\text{CO}_2$ ,  $\text{HCN}$ ,  $\text{CO}$ ,  $\text{H}_2\text{S}$ ,  $\text{NH}_3$ ,  $\text{C}_2\text{H}_2$ ,  $\text{Na}$ ,  $\text{K}$ ,  $\text{TiO}$ , and  $\text{VO}$  as opacity sources in the atmosphere. Additionally,  $\text{H}_2$ - $\text{H}_2$  and  $\text{H}_2$ -He opacities were used as collision induced absorption (CIA) species. For defining the carbon-to-oxygen ratio (C/O), we followed the same prescription as Madhusudhan (2012), Mollière et al. (2015), Woitke et al. (2018), and Molaverdikhani et al. (2019), where the oxygen elemental abundance was altered, but the carbon elemental abundance was maintained at a constant value.

We considered globally averaged insolation treatment for radiative transfer calculation. For cloud treatment, we opted for Ackerman & Marley (Ackerman & Marley 2001) prescription: providing the settling factor ( $f_{\text{sed}} = 2$ ) and lognormal particle distribution width ( $\sigma_g = 1.05$ ).

**Table 1.** Relevant parameters of the WASP-77 A b and WASP-76 b systems

Star Parameters				
WASP-77 A			WASP-76	
Parameters	Values	References	Values	References
$M_*/M_\odot$	1.002	Maxted et al. (2012)	1.460	West et al. (2016)
$R_*/R_\odot$	1.12	Maxted et al. (2012)	1.730	West et al. (2016)
[Fe/H]	0	Maxted et al. (2012)	0.23	West et al. (2016)
$T_*$ (K)	5500	Maxted et al. (2012)	6250	West et al. (2016)
Planet Parameters				
WASP-77 A b			WASP-76 b	
$M_p/M_{\text{Jup}}$	1.759	Maxted et al. (2012)	0.922	West et al. (2016)
$R_p/R_{\text{Jup}}$	1.210	Maxted et al. (2012)	1.877	West et al. (2016)
$\log(g)$	3.477	Southworth et al. (2007)	2.8	Southworth et al. (2007)
$T_{\text{eq}}$ (K)	1715	Cortés-Zuleta et al. (2020)	2160	West et al. (2016)
C/O	0.8	Hoch et al. (2023)	1.2	Hoch et al. (2023)
$a$ (AU)	0.023	Cortés-Zuleta et al. (2020)	0.033	West et al. (2016)
Period (days)	1.36	Ivshina & Winn (2022)	1.81	Ivshina & Winn (2022)
Distance (parsec)	93	Maxted et al. (2012)	120	West et al. (2016)

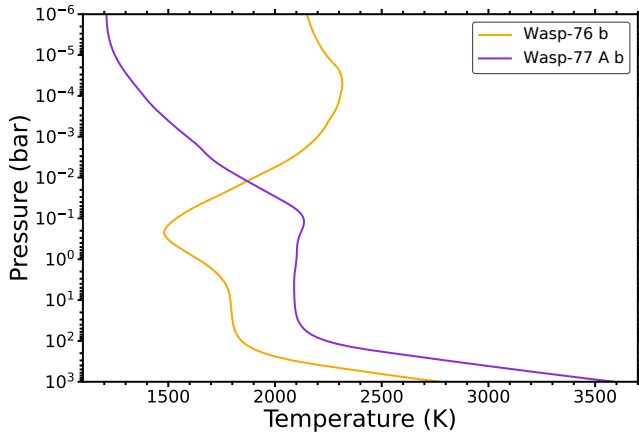


**Figure 2.** Self-consistent PT profile for both planets, simulated with the 1-D radiative-convective equilibrium model, petitCODE, using the system parameters and elemental abundances listed in Table 1. The orange line shows the inverted PT profile for WASP-76 b, whereas the violet one represents the non-inverted PT profile for WASP-77 A b.

## 2.2. Chemical evolution: vertical mixing and photochemistry in action

In our study, we have taken the PT profiles from petitCODE as input for the 1-D chemical kinetics model

VULCAN<sup>4</sup> and then evolved the atmospheric chemistry for both planets. We utilize the original ‘SNCHO photo network’ from the repository, which consists of 1150 reactions connecting 96 different species. Disequilibrium chemistry is effectively incorporated into planet atmospheres by implementing eddy diffusion, molecular diffusion, and photochemical processes. While chemical reactions govern molecular diffusion and photochemistry, eddy diffusion is regulated by the Eddy diffusion coefficient ( $K_{zz}$ ), which is kept constant =  $10^{10}$  cm<sup>2</sup>/s (following the most common value from Tsai et al. (2017)) for both planets. Apart from the star-planet parameters, planet-specific elemental abundances (O/H, N/H, C/H, S/H, and He/H) are also necessary for VULCAN to initiate the equilibrium chemistry calculation using its coupled equilibrium chemistry solver, Fastchem<sup>5</sup> (Stock et al. 2018). We keep the He/H abundance ratio constant at 0.085 and change the remaining abundance values accordingly, following the C/O ratio and metallicity of planets (see Table 1). The C/O ratio influences the elemental abundances of carbon and oxygen specifically (refer to Section 2.1). In contrast, metallicity affects the elemental abundances of all elements. The notation [Fe/H] is used to represent metallicity on a logarithmic scale. Here, [Fe/H] = 0 denotes solar

<sup>4</sup> <https://github.com/exoclimate/VULCAN>

<sup>5</sup> <https://github.com/exoclimate/FastChem>

metallicity,  $[\text{Fe}/\text{H}] = 1$  indicates an elemental abundance ten times greater than solar, and  $[\text{Fe}/\text{H}] = -1$  signifies an elemental abundance ten times lower than solar.

### 2.3. Transmission spectra simulation from planet atmospheres

We couple the time-evolved chemistry from VULCAN to the 1-D radiative transfer model, petitRADTRANS<sup>6</sup>, to simulate high-resolution line-by-line synthetic transmission spectra for both planets at a reference pressure level of  $P_0 = 0.01$  bar. We utilize a customized Python3 wrapper for this purpose. We have considered OH, H<sub>2</sub>O, CO, CO<sub>2</sub> (Rothman et al. 2010), CH<sub>4</sub>, HCN, NH<sub>3</sub>, H<sub>2</sub>S (Chubb et al. 2021) (for WASP-76 b) and OH, H<sub>2</sub>O, CO, CO<sub>2</sub>, NH<sub>3</sub>, H<sub>2</sub>S (for WASP-77 A b) as opacity sources. The selection of chemical species is determined by their average molecular volume mixing ratios (VMRs)  $> 10^{-8}$  at the photospheric level. Molecules with a lower VMR than  $10^{-8}$  would not have a significant impact on the planet’s spectra. Hence, considering other molecules does not add any additional change to the planet’s spectra and hence, to the analysis. The photosphere is the region in the atmosphere that contributes more to the planet’s spectra and lies in the nexus of 1 bar-0.1 mbar region in the atmosphere. In addition, we use CIA opacities for H<sub>2</sub>-H<sub>2</sub> and H<sub>2</sub>-He and H<sub>2</sub> and He as Rayleigh scattering species. The wavelength range and resolution for different spectra are instrument-specific (see Table 2). The default resolution for line-by-line opacities is  $R = 10^6$  in petitRADTRANS. To avoid numerical inefficiency, we downsample the high-resolution molecular opacity files to the spectrograph resolutions before the radiative transfer calculation. For different instrumental resolutions, the rebinning of the opacity files is done using the inbuilt opacity sampling method (by providing the resolution downsampling factor) of petitRADTRANS.

### 2.4. Noise calculation and observation simulation

Ground-based observations pose significant challenges, primarily due to the presence of Earth’s atmosphere. The prominent challenge stems from the interference of telluric lines in the observed spectra, which introduces a caveat when attempting to estimate the molecular fingerprints within the planetary spectrum. To address this issue, we have employed a cutting-edge, coronagraph-free, ground-based noise simulator pipeline, SPECTR<sup>7</sup>, to simulate the observations for both planets using different ground-based instruments. It quantifies the planetary photon count as the signal while considering starlight, zodiacal light, exo-zodiacal light, moon-

light, airglow, instrumental thermal emission, and Earth’s atmosphere (telluric) photon counts as noise sources.

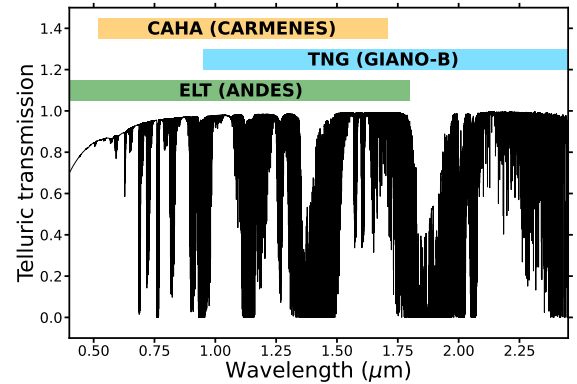


**Figure 3.** Telluric transmission from SkyCalc for the total wavelength coverage of all the instruments: blue band is for TNG (0.95-2.45  $\mu\text{m}$ ), orange band for CAHA (0.52-1.71  $\mu\text{m}$ ), and green band for ELT (0.4-1.8  $\mu\text{m}$ ). The telluric lines were calculated for the resolution  $R = 80000$ . It shows the differential effect of telluric lines on the instrumental wavelength coverages. While similar telluric lines impact CARMENES and ANDES observations, GIANO-B has some influence at the longer wavelengths.

SPECTR is integrated with the state-of-the-art atmospheric telluric model, Cerro Paranal Advanced Sky Model (SkyCalc)<sup>8</sup> (Noll et al. 2012), from the European Southern Observatory for simulating wavelength-dependent background and telluric lines at the resolution specific to the instrument. In line with the approach outlined in the (Currie et al. 2023), we have selected Paranal as the observatory location and assumed a precipitable water vapor level of 3.5 mm for calculating Earth’s atmospheric telluric lines. Observed telluric transmission at the site of observation is shown in Figure 3. The read noise and dark current values for different instruments are listed in Table 2. We have set the exposure duration equal to 488 seconds for each target, following the WASP-76 b observations by Landman et al. (2021) and Sánchez-López et al. (2022) using CARMENES spectrograph. We have kept the same exposure time for all the spectrographs to estimate a comparative understanding of the instrumental capability of molecular detection.

It is important to note that we have assumed a consistent throughput of 21% for GIANO-B (Oliva et al. 2006), 7.9% for CARMENES (Seifert et al. 2016), and 10% for ANDES (Currie et al. 2023). Throughputs are usually wavelength-dependent. However, the measurements of instrumental throughputs are limited to certain wavelength points. To overcome this issue, we have considered the best throughput

<sup>6</sup> <https://petitradtrans.readthedocs.io/en/latest/>

<sup>7</sup> <https://github.com/curriem/spectr>

<sup>8</sup> <https://www.eso.org/observing/etc/doc/skycalc/helpskycalcli.html>

**Table 2.** Instrumental configuration for three ground-based observatories

Telescope/ Instrument	Wavelength ( $\mu\text{m}$ )	Resolution	Diameter (m) (m)	Read Noise ( $e^-$ )	Dark Current ( $e^-/\text{pixel/s}$ )	$T_{\text{opt}}$ (K)
TNG (GIANO-B)	0.95-2.45	50000	3.58	5	0.05	50
CAHA (CARMENES)	0.52-1.71	80000	3.5	13.52	0.002	140
ELT (ANDES)	0.4-1.8	100000	39.3	3	0.00056 (optical) 0.0011 (NIR)	143

<sup>a</sup> Note: The instrumental parameters are taken from the respective websites of the high-resolution spectrographs. GIANO-B: <https://www.tng.iac.es/instruments/giano-b/>. CARMENES: <https://www.caha.es/telescope-3-5m/carmenes>. ANDES: <https://elt.eso.org/instrument/ANDES/>.

value for the spectrographs. Hence, our assumption serves as an upper limit for molecular detection from the perspective of the instrumental throughput parameter. For telescope mirror temperature, we have followed (Currie et al. 2023) and maintained a consistent temperature of 273 K across all observatories. But the detector temperatures ( $T_{\text{opt}}$ ) are set according to the specifications outlined in Table 2. Different sources of noise components are shown in Figure 4. Furthermore, for uniformity, we have designated 100 detector pixels per resolution for all the detectors and carried out the observation for 1 and 3 transits for both planets (following the observations on hot gas giant planets by Sánchez-López et al. (2020), Landman et al. (2021), Sánchez-López et al. (2022), Carleo et al. (2022), Borsato et al. (2024), and Prinoth et al. (2024)).

The pipeline Doppler shifts the planet’s spectrum and multiplies the telluric lines at each exposure to it. The systematic radial velocity shifts relative to Earth are taken to be  $-1.07 \text{ km s}^{-1}$  for WASP-76 b (West et al. 2016) and  $1.68 \text{ km s}^{-1}$  for WASP-77 A b (Maxted et al. 2012). The pipeline systematically includes out-of-transit observations alongside each in-transit observation to facilitate the precise isolation of the planet signal and noise within observed transmission spectra. To enhance data quality, the pipeline employs an outlier mask and high-pass filters to eliminate data points with exceptionally low signal-to-noise ratios and mitigate low-frequency variations.

It computes the detection significance ( $\sigma_{\text{det}}$ ) of molecular bands using the cross-correlation spectroscopy technique as outlined in (Brogi et al. 2016). This method exhibits a high degree of sensitivity to line features and demonstrates robustness even in the presence of minimal perturbations in radial velocity. Our approach involves cross-correlating the simulated spectra ( $f(\lambda)$ ) for both planets with Doppler-shifted template spectra ( $f(\lambda - \lambda')$ ) representing various molecular bands and, thus, calculating the detectability of these molecules across a range of ground-based facilities operating at different resolutions and different wavelength regimes. Here,  $\lambda$  denotes the bin number, while  $\lambda'$  signifies the bin

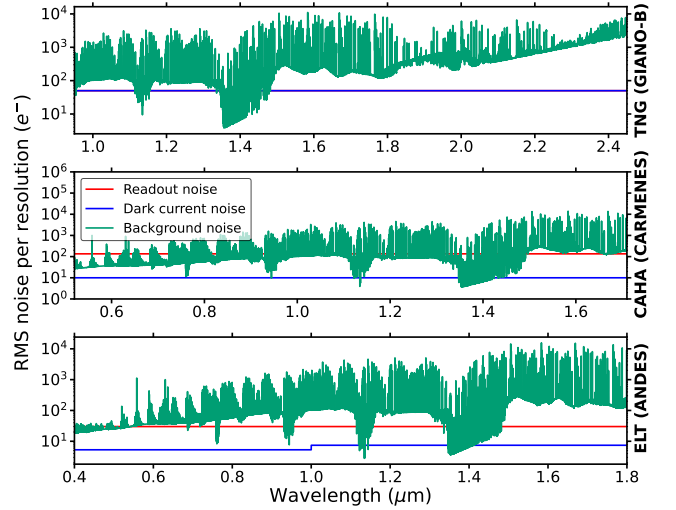


**Figure 4.** Different noise sources in the visible and NIR region for different instruments: 1. Background noise (telluric emission + thermal emission of instrument + zodiacal light + airglow) (bluish-green) 2. Readout noise (red), and 3. Dark current noise (blue). The noises are measured for an exposure duration of 488 seconds at native resolutions specific to instruments (see Table 2). It shows the variability of background noise over a wide wavelength span, the different instrumental read-out noise, and the dark current values. Overall, it presents the differential influence of noise profiles on different telescopic observations. The step function observed in the Dark current noise for the ELT arises from the distinct dark current counts in the optical and NIR regions. For TNG, the values for readout noise and dark current noise are the same.

shift attributable to relative velocity. To generate velocity-shifted template spectra, we opt for an extensive grid of Doppler velocities, spanning from  $-150 \text{ km s}^{-1}$  to  $+150 \text{ km s}^{-1}$ , with 101 intervals. Here, we will brief the numerical recipe to compute the  $\sigma_{\text{det}}$  following (Currie et al. 2023) (for more details see Brogi & Line (2019)):

$$s_f^2 = \frac{1}{N} \sum_{\lambda} f^2(\lambda), s_f^2 = \text{variance of the observed spectrum} \quad (1)$$

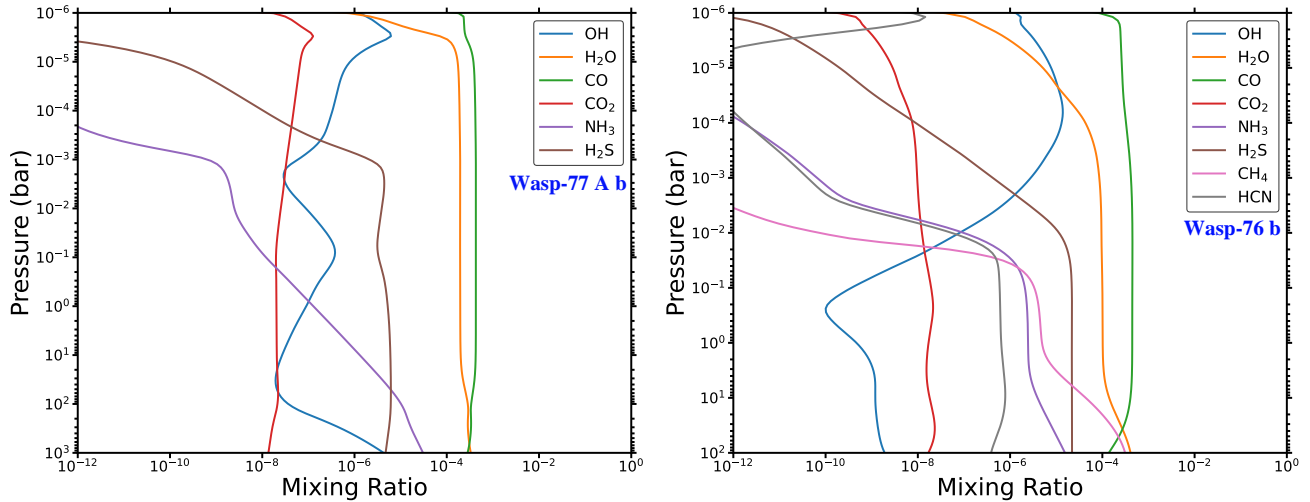


**Figure 5.** Mixing ratio profiles from VULCAN for specific molecules in the atmosphere of both planets. WASP-77 A b (left): OH, H<sub>2</sub>O, CO, CO<sub>2</sub>, NH<sub>3</sub>, H<sub>2</sub>S, and WASP-76 b (right): OH, H<sub>2</sub>O, CO, CO<sub>2</sub>, NH<sub>3</sub>, H<sub>2</sub>S, CH<sub>4</sub>, HCN. Molecules are selected considering the average mixing ratios  $> 10^{-8}$  between the 1 bar-0.1 mbar pressure layers (photosphere).

$$s_{\text{g}}^2 = \frac{1}{N} \sum_{\lambda} f^2(\lambda - \lambda'), \quad s_{\text{g}}^2 = \text{variance of the template spectrum} \quad (2)$$

where  $N$  is the total number of pixels. Hence, the cross-covariance can be defined as

$$R(\lambda) = \frac{1}{N} \sum_{\lambda} f(\lambda)f(\lambda - \lambda') \quad (3)$$

Now, Eqs. 1, 2, and 3 can be coupled together to estimate the cross-correlation function (CCF) ( $C(\lambda)$ ), which peaks at the relative velocity of zero for a detectable planetary signal

$$C(\lambda) = \frac{R(\lambda)}{\sqrt{s_{\text{f}}^2 s_{\text{g}}^2}} \quad (4)$$

Thereafter, a  $\chi^2$  analysis is followed between estimated CCF and a flat line to test for a signal (Brogi et al. 2016)

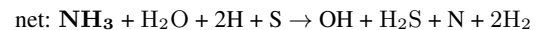
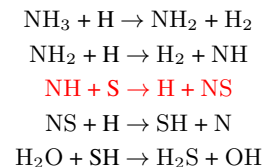
$$\chi_{\text{CCF}}^2 = \sum_{\lambda} \frac{[C(|\lambda| < \lambda_0) - 0]^2}{\sigma_{C(|\lambda| > \lambda_0)}^2} \quad (5)$$

In Eq. 5, the  $\chi_{\text{CCF}}^2$  is summed over the velocity shifts ( $|\lambda|$ ) less than  $\lambda_0 = 5 \text{ km s}^{-1}$ . These values only represent the planet signal in the calculation and the typical width of the CCF peak. The denominator, on the other hand, signifies the variance, excluding any potential planetary signals. Utilizing the cumulative  $\chi^2$  distribution function and inverse survival function of a normal distribution,  $\chi_{\text{CCF}}^2$  is converted to  $p$ -value and later on, to a sigma interval. Finally,  $\sigma_{\text{det}}$  is estimated as a measure of the deviation of the CCF from a Gaussian distribution.

### 3. RESULTS

#### 3.1. High-resolution transmission spectra: linking molecular VMRs to their spectral signatures

As discussed in Section 2.3, the determination of molecules for simulating synthetic high-resolution spectra depends on their average VMRs  $> 10^{-8}$  in the planetary photosphere. The criterion leads us to the inclusion of OH, H<sub>2</sub>O, CH<sub>4</sub>, CO, CO<sub>2</sub>, HCN, NH<sub>3</sub>, H<sub>2</sub>S in the atmosphere of WASP-76 b and OH, H<sub>2</sub>O, CO, CO<sub>2</sub>, NH<sub>3</sub>, H<sub>2</sub>S in the atmosphere of WASP-77 A b. The molecular VMRs for both planets have been showcased in Figure 5. The atmospheric compositions of the planets are significantly influenced by CO and H<sub>2</sub>O, with H<sub>2</sub>S also showing a considerable presence in both of them. It is worth mentioning that at a pressure level of  $\sim 0.01$  bar, the VMR of OH starts rising for both planets, and this can be attributed to the reduction in levels of H<sub>2</sub>O and, in particular, NH<sub>3</sub> (see Figure 6). They both contribute  $\sim 74\%$  (for WASP-76 b) and  $\sim 99\%$  (for WASP-77 A b) to the net OH formation at the specific pressure level. While H<sub>2</sub>O undergoes a single reaction:  $\text{H}_2\text{O} + \text{H} \rightarrow \text{OH} + \text{H}_2$  for the conversion, NH<sub>3</sub> has different routes to form OH. For WASP-76 b, the fastest interconversion follows the path



whereas, for WASP-77 A b it undergoes

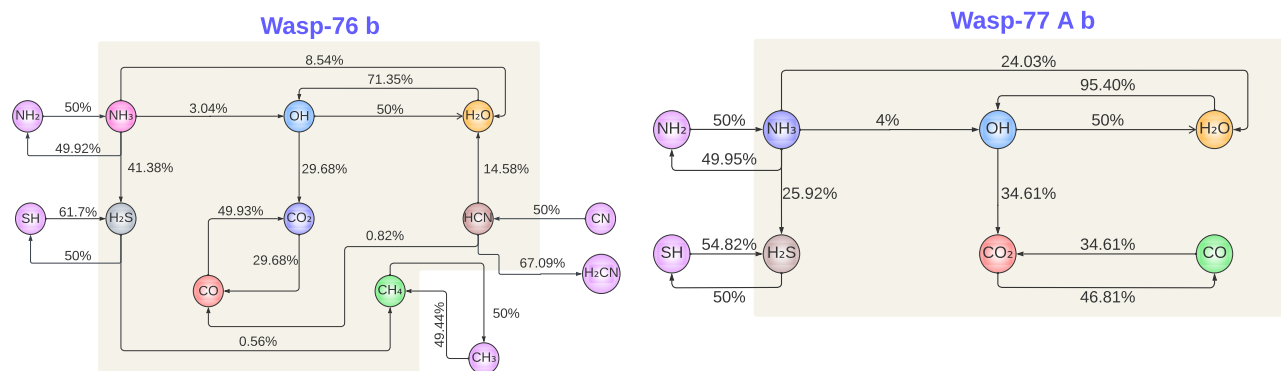


**Figure 6.** Illustration of the principal chemical pathways and their conversion rates at a pressure level of 0.01 bar (consistent with the photosphere) for specific molecules. *Left panel:* WASP-76 b. *Right panel:* WASP-77 A b. The “tan” shaded areas represent molecules with an average VMR  $> 10^{-8}$  between 1 bar–0.1 mbar (photosphere). Molecules outside these ‘tan’ regions, indicated by ‘magenta’ circles, are non-significant in terms of VMR, but they serve as crucial sources and sinks for some molecules. For detailed model-specific analyses of reaction pathways, including the incorporation of all secondary reactants, see Figures 11, 12 in the Appendix A.

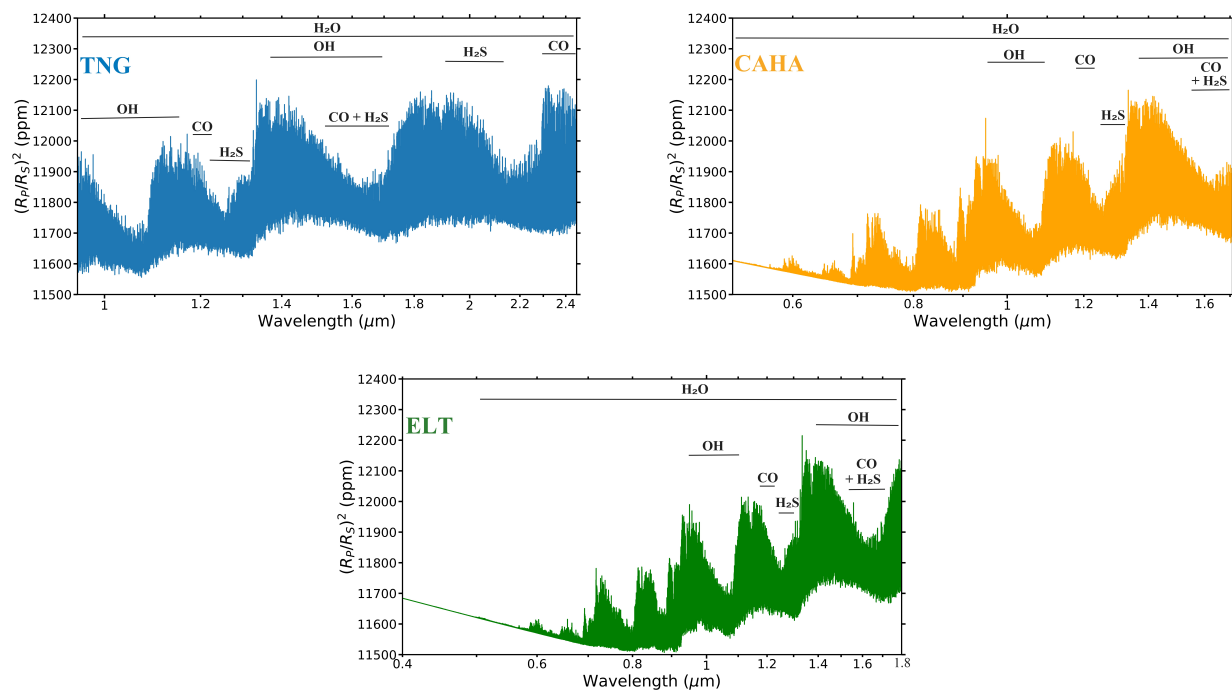


**Figure 7.** High-resolution transmission spectra of WASP-77 A b for different instruments (see instrumental parameters from Table 2). *Blue:* GIANO-B (TNG). *Orange:* CARMENES (CAHA). *Green:* ANDES (ELT). The figure illustrates the contributions from different molecular bands to the net planet spectra for all cases. Despite having a significant average photospheric VMR, discernible  $\text{CO}_2$  and  $\text{NH}_3$  features are not present in any of the synthetic spectra.



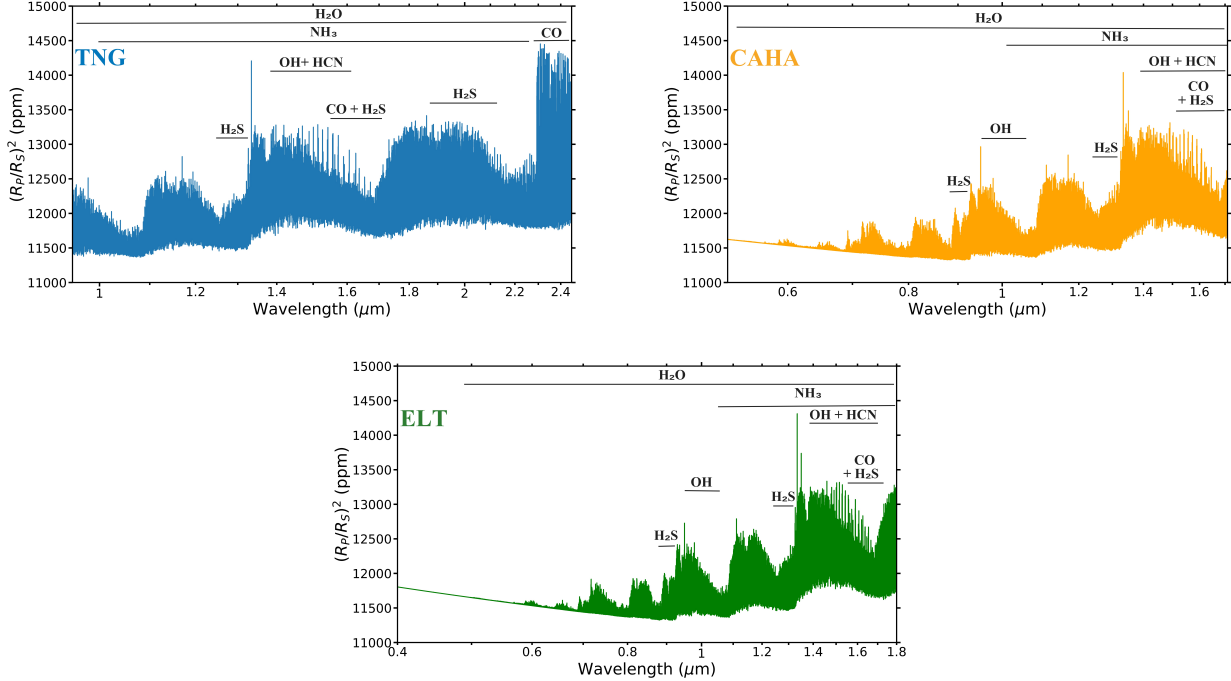
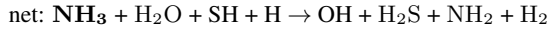
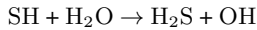
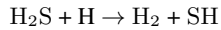


**Figure 8.** High-resolution transmission spectra of WASP-76 b for different instruments (see instrumental parameters from Table 2). *Blue*: GIANO-B (TNG). *Orange*: CARMENES (CAHA). *Green*: ANDES (ELT). The figure illustrates the contributions from different molecular bands to the net planet spectra for all cases. Despite having significant average photospheric VMRs, discernible  $\text{CH}_4$  and  $\text{CO}_2$  features are not present in any of the synthetic spectra.



The reactions in red colors indicate the rate-limiting steps for the whole reaction pathways. On the other hand, a large amount of  $\text{NH}_3$  gets converted to  $\text{H}_2\text{S}$  and  $\text{H}_2\text{O}$ , leading to a further reduction in  $\text{NH}_3$  concentration on both planets. A similar story for  $\text{HCN}$  has been observed too on WASP-76 b, producing  $\text{H}_2\text{O}$  and  $\text{H}_2\text{CN}$  significantly. Figure 6, which provides a robust visual representation of chemical networks for both planets, emphasizes this fact further. The figure highlights the molecular interconversions, with their net percentage contribution to the formation and destruction of other molecules. Types of reaction intermediates that participate in the fastest molecular conversion pathway are shown in Figures 11 and 12. The shortest route for molecular interconversions is built upon the principle of Dijkstra’s algorithm (the principle of finding the least distance between two nodes in a complex network with other nodes present in between) (Dijkstra 2022) and is adopted from Tsai et al. (2018). While not being present significantly in the atmospheres,  $\text{NH}$ ,  $\text{SH}$ ,  $\text{NS}$ , and  $\text{NH}_2$  play very crucial roles in the interconversions (see Appendix A).

Figures 7 and 8 present synthetic spectra for WASP-77 A b and WASP-76 b, respectively, showcasing their spectral characteristics. These models are generated at the resolutions and wavelength ranges corresponding to the TNG (GIANO-B), CAHA (CARMENES), and ELT (ANDES) instruments. The figures also illustrate the molecular contributors responsible for various spectral features. It is noteworthy that WASP-77 A b lacks discernible  $\text{NH}_3$  and  $\text{CO}_2$  features, while WASP-76 b exhibits an absence of  $\text{CH}_4$  and  $\text{CO}_2$  features in their respective spectra. This is due to the prominent features of other molecules, coupled with the lower abundance of the respective molecules.

### 3.2. Cross-correlation spectroscopy: estimation of $\sigma_{\text{det}}$ for molecular bands

In our analysis, assessing the detectability of molecular signatures presents a unique challenge, primarily arising from the complex spectral profiles characterized by more spectral lines present in the spectrum. Unlike the conventional signal-to-noise ratio (S/N) estimation, where a non-detection typically results in an S/N of zero, our approach yields a non-detection consistent with a significance level of  $\sigma_{\text{det}} \sim 1$  (Currie et al. 2023). This deviation from the traditional methodology is driven by the intricacies of our detection scheme, which accounts for the complex nature of the spectral lines and their interactions, making our scheme a

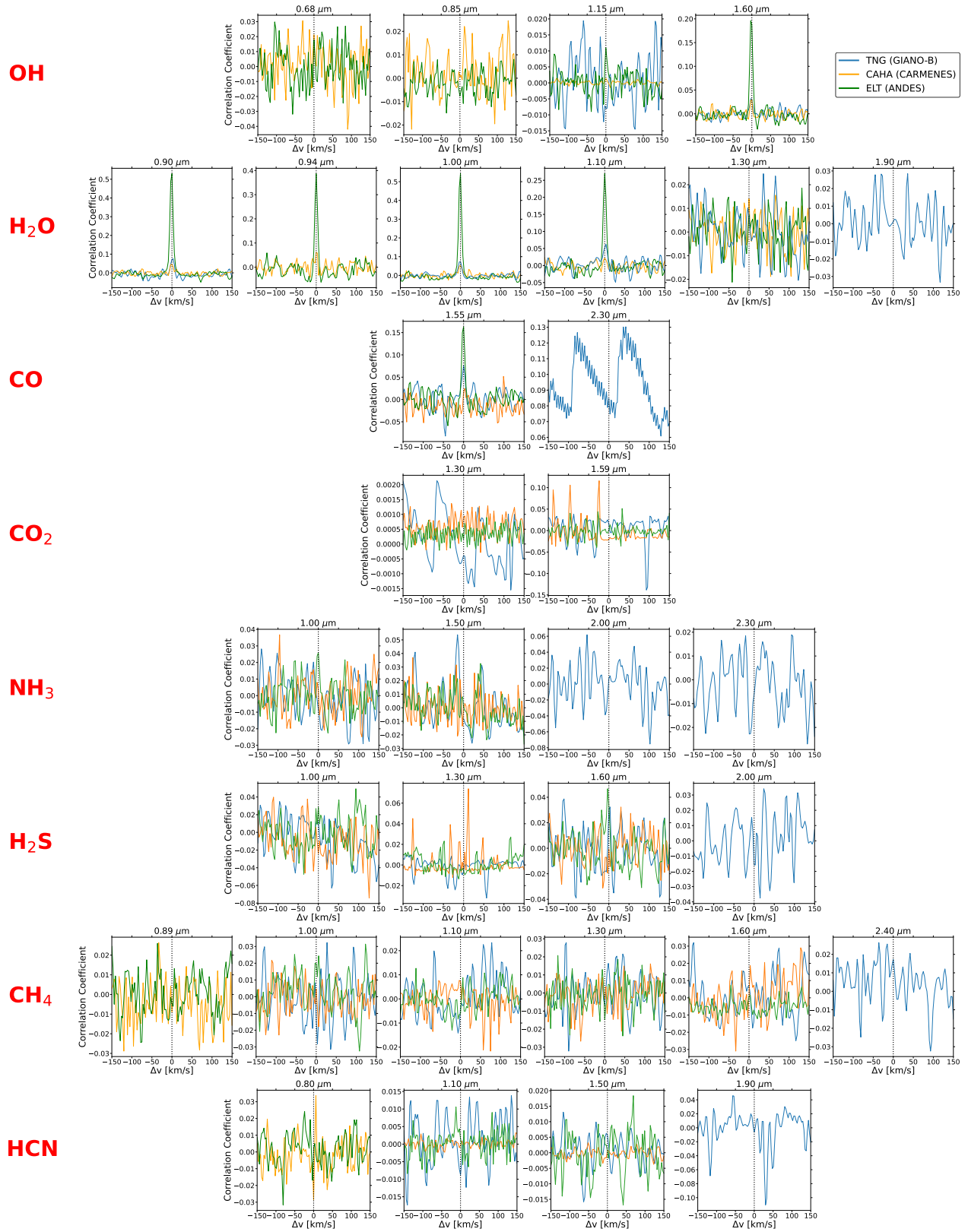


**Figure 9.** Correlation coefficient vs. velocity shift map for different molecular bands for 3 transits of WASP-76 b. *Blue:* GIANO-B (TNG). *Orange:* CARMENES (CAHA). *Green:* ANDES (ELT). Each row corresponds to a specific molecule (*from top to bottom:* OH, H<sub>2</sub>O, CH<sub>4</sub>, CO, CO<sub>2</sub>, HCN, NH<sub>3</sub>, H<sub>2</sub>S). Molecular bands are listed explicitly in Table 3.

**Table 3.** Table summarizing the  $\sigma_{\text{det}}$  achieved for different molecular bands for different number of transits of WASP-76 b from different ground-based instruments (bands with  $\sigma_{\text{det}} > 3$  are shown in bold)

Molecules	Bands ( $\mu\text{m}$ )	Wavelength range ( $\mu\text{m}$ )	No. of transit = 1			No. of transit = 3		
			TNG (GIANO-B)	CAHA (CARMENES)	E-ELT (ANDES)	TNG (GIANO-B)	CAHA (CARMENES)	E-ELT (ANDES)
OH	0.68	0.66 - 0.70	–	No detection	No detection	–	No detection	No detection
	0.85	0.77 - 0.93	–	No detection	No detection	–	No detection	No detection
	1.15	1.0 - 1.3	No detection	No detection	2.36	No detection	3.06	3.31
	1.60	1.5 - 1.7	3.98	3.23	12.87	4.66	4.41	14.75
H <sub>2</sub> O	0.90	0.89 - 0.99	6.35	5.10	19	6.68	5.64	19.12
	0.94	0.93 - 0.95	–	1.96	13.17	–	3.27	14.45
	1.00	0.95 - 1.05	3.58	1.21	18.57	8.64	4.54	19.94
	1.10	1.1 - 1.2	3.01	No detection	15.87	3.34	No detection	17.63
	1.30	1.3 - 1.55	No detection	No detection	No detection	No detection	No detection	No detection
	1.90	1.8 - 2.1	No detection	–	–	No detection	–	–
CO	1.55	1.555 - 1.60	2.36	1.24	9.38	3.15	2.10	10.34
	2.30	2.319 - 2.3315	No detection	–	–	No detection	–	–
CO <sub>2</sub>	1.30	1.2 - 1.4	No detection	No detection	No detection	No detection	No detection	No detection
	1.59	1.45 - 1.66	No detection	No detection	No detection	No detection	No detection	No detection
NH <sub>3</sub>	1.00	1.0 - 1.1	No detection	No detection	3.83	1.97	1.71	4.29
	1.50	1.45 - 1.65	No detection	No detection	No detection	No detection	No detection	No detection
	2.00	2.0 - 2.1	No detection	–	–	No detection	–	–
	2.30	2.2 - 2.4	No detection	–	–	No detection	–	–
H <sub>2</sub> S	1.00	1.0 - 1.03	No detection	No detection	No detection	No detection	No detection	No detection
	1.30	1.27 - 1.37	No detection	No detection	No detection	No detection	No detection	No detection
	1.60	1.55 - 1.66	1.85	No detection	3.46	3.18	No detection	4.35
	2.00	1.9 - 2.1	No detection	–	–	No detection	–	–
CH <sub>4</sub>	0.89	0.875 - 0.91	–	No detection	No detection	–	No detection	No detection
	1.00	0.98 - 1.05	No detection	No detection	1.41	1.78	No detection	2.26
	1.10	1.1 - 1.2	No detection	No detection	No detection	No detection	No detection	No detection
	1.30	1.3 - 1.55	No detection	No detection	No detection	No detection	No detection	No detection
	1.60	1.6 - 1.8	No detection	No detection	1.16	No detection	No detection	2.70
	2.40	2.2 - 2.5	No detection	–	–	No detection	–	–
HCN	0.80	0.8 - 0.9	–	No detection	1.07	–	2.42	2.65
	1.10	1.0 - 1.2	No detection	No detection	No detection	No detection	No detection	No detection
	1.50	1.47 - 1.56	No detection	No detection	No detection	No detection	No detection	No detection
	1.90	1.85 - 1.95	No detection	–	–	No detection	–	–

more appropriate means of determining detectability in this context.

Therefore, our approach involves a more detailed analysis rather than employing the conventional S/N estimator, which provides a detectability estimate for the entire wavelength range. We have defined specific molecular bands corresponding to each molecule of interest (see Table 3 and 4) and provided an overview in terms of  $\sigma_{\text{det}}$  for each of the molecular bands using three different spectrographs for 1 and 3 transits, respectively. This approach allows us to assess the detectability of individual molecular features within the broader spectrum, providing a more detailed and accurate characterization of their presence in a better way. In the subsequent sections, we have discussed a comprehensive analysis of detecting various molecular bands on both planets using all the instruments. Transit depths for all bands are shown in Figures 13, 14, 15 (for WASP-76 b) and Figures 16, 17, 18 (for WASP-77 A b). The cross-correlation spectroscopy for molecular bands has been depicted in Figures 9 and 10, where a clear detection is indicated by a pronounced peak at zero velocity shift in the correlation coefficient vs. velocity shift map.

### 3.2.1. OH

OH is one of the major byproducts that have formed during the atmospheric dissociation of  $\text{H}_2\text{O}$  (Landman et al. 2021). For HJs and UHJs, the enrichment of OH at the top of the atmosphere can be attributed to the photolysis of water molecules. It was proven during the detection of OH (with a  $5.5\sigma$  significance) on Wasp-33 b, where the insignificant detection of  $\text{H}_2\text{O}$  lends support to the hypothesis that OH formation is facilitated by the thermal dissociation of  $\text{H}_2\text{O}$  molecules (Nugroho et al. 2021). However, from Figure 6, it is evident that  $\text{H}_2\text{O}$  does play a substantial role in the generation of OH radicals through the following reaction:  $\text{H}_2\text{O} + \text{H} \rightarrow \text{OH} + \text{H}_2$  (see Figure 11 and 12), but not with direct photolysis. A more detailed understanding of this necessitates further exploration, which can be achieved through the utilization of more intricate chemical networks.

For WASP-76 b, all spectrographs demonstrate superior sensitivity in probing the  $1.60 \mu\text{m}$  band. While achieving a better  $\sigma_{\text{det}}$  requires more transits for GIANO-B and CARMENES, ANDES is capable of reaching a commendable  $\sigma_{\text{det}}$  within 1 transit. Additionally, CARMENES and ANDES exhibit significant precision in detecting the  $1.15 \mu\text{m}$  band with a higher number of transits. Similarly, in the case of WASP-77 A b, ANDES exhibits reasonable precision in detecting the  $1.15 \mu\text{m}$  and  $1.60 \mu\text{m}$  features with an increased number of transits. However, it's worth noting that ANDES exhibits a lower level of confidence for detecting the  $1.60 \mu\text{m}$  band compared to the observations of WASP-76 b.

### 3.2.2. $\text{H}_2\text{O}$

From the planet spectra, it is clear that both planets are water-dominated. Among all six bands, the  $0.90$ ,  $1.00$ , and  $1.10 \mu\text{m}$  bands in the optical and NIR spectral regions exhibit notably higher precision across three instruments for a higher number of transits. It is important to note that ANDES demonstrates superior capability in containing these features even with a single transit. Both CARMENES and ANDES exhibit favorable detectability for the  $0.94 \mu\text{m}$  band too. All over, CARMENES shows a lower level of sensitivity towards detecting different bands. This is attributed to the higher read noise value of the spectrograph and the lower collecting area of the mirror.

In our analysis, the  $0.90$ ,  $0.94$ ,  $1.00$ , and  $1.10 \mu\text{m}$  bands have proven to be more dependable in terms of detection. Although the  $1.30 \mu\text{m}$  band exhibits pronounced features, they are susceptible to overlap with the prominent telluric transmission features, resulting in reduced significance during detection. A similar effect is also observed for the  $1.10 \mu\text{m}$  band, albeit to a lesser extent.

### 3.2.3. CO

CO emerges as the predominant molecule in terms of VMR on both planets (see Figure 5). It is produced mainly by the direct reduction  $\text{CO}_2$  molecule in the atmospheres:  $\text{CO}_2 + \text{H} \rightarrow \text{CO} + \text{OH}$  (see Figure 6 and Appendix A). GIANO-B and ANDES exhibit potential in detecting the  $1.55 \mu\text{m}$  band with  $\sigma_{\text{det}} > 3$  in the atmosphere of WASP-76 b (GIANO-B: with 3 transits and ANDES: with a single transit). Moreover, the detection of CO on WASP-77 A b is insignificant with GIANO-B and CARMENES with a  $\sigma_{\text{det}} < 3$  even with 3 transits. ANDES can achieve a significance level of  $\sigma_{\text{det}} > 3$  for the  $1.55 \mu\text{m}$  CO band when observing for 3 transits. The detectability increases in the sequence from CARMENES to GIANO-B to ANDES.

### 3.2.4. $\text{CO}_2$

With a threshold of average photospheric VMR  $> 10^{-8}$ , it is apparent that  $\text{CO}_2$  is the least abundant species on both planets. Unfortunately, neither of its bands is detectable for all instruments.

### 3.2.5. $\text{NH}_3$

As previously discussed in Section 3.1, the contribution of  $\text{NH}_3$  to the planetary spectra is not visually distinguishable for WASP-77 A b, indicating a minimal likelihood of detection. ANDES exhibits reasonable detection significance for WASP-77 A b for the  $1.00 \mu\text{m}$  band. Nevertheless, it demands more transits to achieve a significant detection. In contrast, for WASP-76 b, the ANDES instrument is capable of resolving the  $1.00 \mu\text{m}$  band with higher precision ( $\sigma_{\text{det}} > 3$ ) even with a single transit.

### 3.2.6. $\text{H}_2\text{S}$

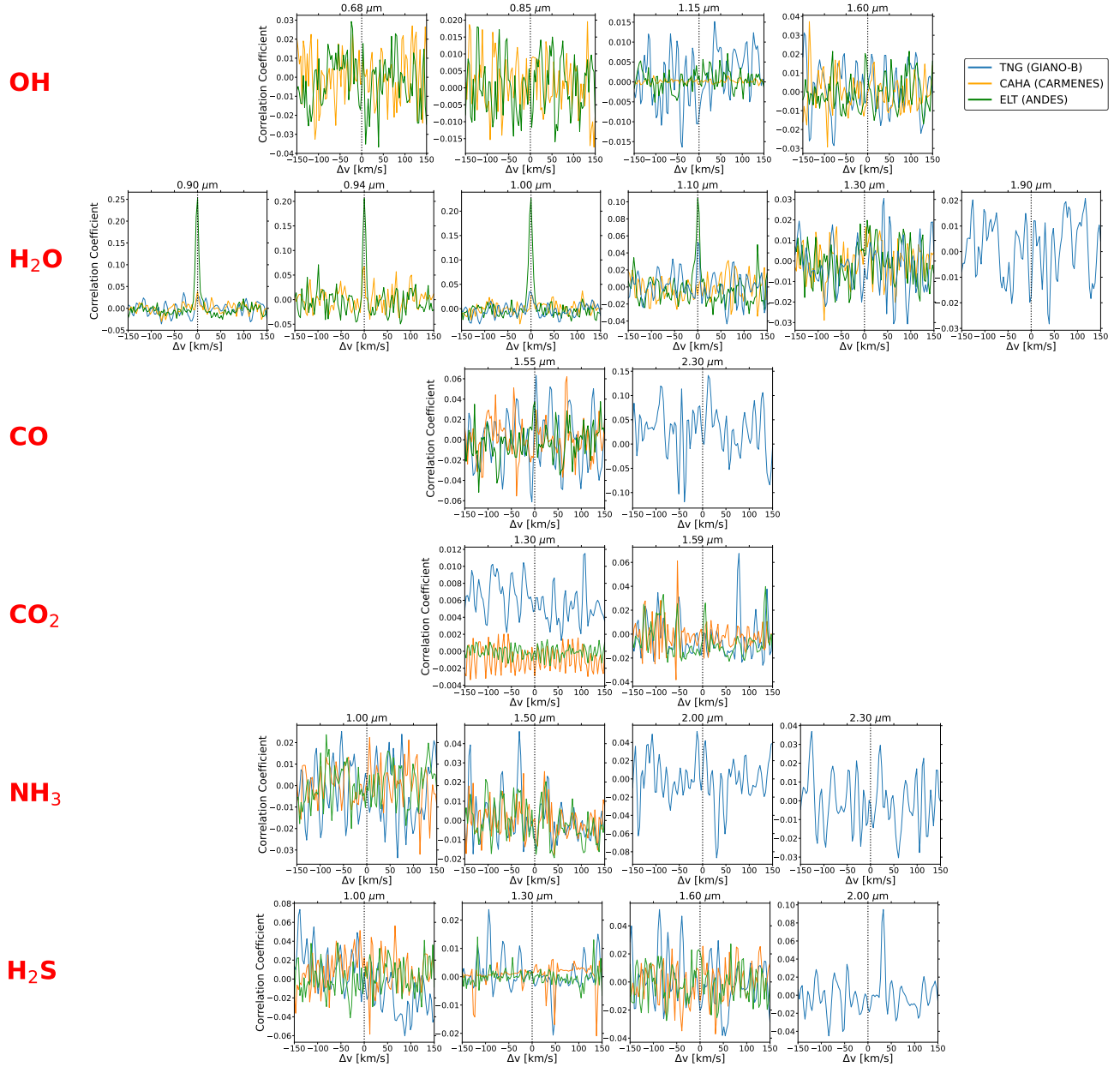


**Figure 10.** Correlation coefficient vs. velocity shift map for different molecular bands for 3 transits of WASP-77 A b. *Blue:* GIANO-B (TNG). *Orange:* CARMENES (CAHA). *Green:* ANDES (ELT). Each row corresponds to a specific molecule (*from top to bottom:* OH, H<sub>2</sub>O, CO, CO<sub>2</sub>, NH<sub>3</sub>, H<sub>2</sub>S). Molecular bands are listed explicitly in Table 4.

On both studied planets, sulfur is exclusively found in the form of H<sub>2</sub>S. Despite being the third most prevalent compound in their atmospheres, no prior detection has been recorded for this molecule. Our analysis, however, indicates a substantial detection of the 1.60  $\mu\text{m}$  band on WASP-76 b and a moderate level of detection on WASP-77 A b, using the ANDES instrument. With additional transits, GIANO-B too shows prominence in detecting the 1.60  $\mu\text{m}$  band on WASP-76 b. The significant formation of this molecule in the atmosphere can be attributed to the destruction NH<sub>3</sub> and SH radical (see Figure 6 and Appendix A).

### 3.2.7. CH<sub>4</sub>

Detecting CH<sub>4</sub> is particularly challenging across all three instruments due to its extremely low atmospheric abundance on WASP-76 b. Nevertheless, ANDES displays a little promising capability in detecting the 1.00 and 1.60  $\mu\text{m}$  bands with 3 transits, each with a  $\sigma_{\text{det}} > 2$ . However, none of these instruments exhibits a distinct, sharp feature in the correlation coefficient vs. velocity shift map.

### 3.2.8. HCN

**Table 4.** Table summarizing the  $\sigma_{\text{det}}$  achieved for different molecular bands for different number of transits of WASP-77 A b from different ground-based instruments (bands with  $\sigma_{\text{det}} > 3$  are shown in bold)

Molecules	Bands ( $\mu\text{m}$ )	Wavelength range ( $\mu\text{m}$ )	No. of transit = 1			No. of transit = 3		
			TNG (GIANO-B)	CAHA (CARMENES)	E-ELT (ANDES)	TNG (GIANO-B)	CAHA (CARMENES)	E-ELT (ANDES)
OH	0.68	0.66 - 0.70	–	No detection	No detection	–	No detection	No detection
	0.85	0.77 - 0.93	–	No detection	No detection	–	No detection	No detection
	1.15	1.0 - 1.3	No detection	No detection	No detection	No detection	No detection	2.02
	1.60	1.5 - 1.7	No detection	No detection	No detection	No detection	No detection	2.76
H <sub>2</sub> O	0.90	0.89 - 0.99	2.49	2.10	13.04	3.44	3.30	18.77
	0.94	0.93 - 0.95	–	1.74	5.76	–	4.53	10.52
	1.00	0.95 - 1.05	1.56	1.50	12.85	4.56	3.70	15.52
	1.10	1.1 - 1.2	2.56	No detection	5.45	4.87	No detection	7.89
	1.30	1.3 - 1.55	No detection	No detection	No detection	No detection	No detection	No detection
	1.90	1.8 - 2.1	1.63	–	–	2.98	–	–
CO	1.55	1.555 - 1.60	1.55	1.16	1.92	2.75	1.93	3.49
	2.30	2.319 - 2.3315	No detection	–	–	No detection	–	–
CO <sub>2</sub>	1.30	1.2 - 1.4	No detection	No detection	No detection	No detection	No detection	No detection
	1.59	1.45 - 1.66	No detection	No detection	No detection	No detection	No detection	No detection
NH <sub>3</sub>	1.00	1.0 - 1.1	No detection	No detection	No detection	No detection	No detection	2.61
	1.50	1.45 - 1.65	No detection	No detection	No detection	No detection	No detection	No detection
	2.00	2.0 - 2.1	No detection	–	–	No detection	–	–
	2.30	2.2 - 2.4	No detection	–	–	No detection	–	–
H <sub>2</sub> S	1.00	1.0 - 1.03	No detection	No detection	No detection	No detection	No detection	No detection
	1.30	1.27 - 1.37	No detection	No detection	No detection	No detection	No detection	No detection
	1.60	1.55 - 1.66	No detection	No detection	1.72	No detection	No detection	2.11
	2.00	1.9 - 2.1	No detection	–	–	No detection	–	–

Despite having a prominent detection on WASP-76 b, our model falls short of establishing a sufficient detection of HCN in the atmosphere, leading to the following conclusion: it is anticipated that HCN will originate in the lower temperature region of the planetary nightside and subsequently migrate to the dayside via atmospheric circulation. Given the higher detection significance of H<sub>2</sub>O, the presence of HCN is intriguing, as H<sub>2</sub>O and HCN are not typically expected to coexist (Sánchez-López et al. 2022). However, HCN can be detected to some extent with an increased number of transits on WASP-76 b. Notably, the CARMENES and ANDES instruments demonstrate a reasonable capability to resolve the 0.80  $\mu\text{m}$  band with a detection significance  $\sigma_{\text{det}} > 2$ .

### 3.3. Present observations and the future with ELT

Recent advancements in ground-based observatories have opened up new horizons in the field of exoplanetary science, particularly exploring planet atmospheres and comprehend-

ing the underlying atmospheric chemistry. By comparing present observations with simulation studies, we can anticipate future observations using more advanced instruments like ELT and gain insights into how ELT will excel the existing instruments in detecting molecular signatures in planetary atmospheres. Our model exhibits good coherence with the present observations for both planets. On WASP-76 b, Landman et al. (2021) detect OH with a significance of 6.1, while Sánchez-López et al. (2022) report the detection of H<sub>2</sub>O (with a significance of 5.5) and HCN (with a significance of 5.2) using the CARMENES spectrograph during a single transit observation. We successfully retrieve H<sub>2</sub>O signature from the 0.90  $\mu\text{m}$  band with a  $\sigma_{\text{det}}$  of 5.10 and OH from the 1.60  $\mu\text{m}$  band with a little lower  $\sigma_{\text{det}}$  of 3.23 for single transit. As discussed in Section 3.2.8, the production of HCN is more favorable in the cooler regions of the planet. Due to the limitations imposed by 1D models, we are unable to attain a significant VMR of HCN on the planet and detect

it solely through single transit observations. However, with 3 transits, CARMENES can detect the  $0.80 \mu\text{m}$  band of HCN with a  $\sigma_{\text{det}}$  of 2.42.

On the other hand, observations conducted during pre and post-eclipse of WASP-77 A b using the IGRINS spectrograph indicate the presence of CO (with a significance  $\sim 3.5$ ) and  $\text{H}_2\text{O}$  (with a significance  $\sim 9$ ) in the atmosphere (Smith et al. 2024). Our analysis utilizing GIANO-B and CARMENES also detects CO and  $\text{H}_2\text{O}$ , albeit with slightly lower significance levels for three transits. This is due to the differential spectrograph architectures between GIANO-B, CARMENES, and IGRINS. Specifically, the IGRINS spectrograph has a larger mirror diameter of 8.1 meters compared to 3.58 meters for GIANO-B and 3.5 meters for CARMENES. This larger diameter translates to a doubling in collecting area, leading to a greater influx of photons and consequently enhancing detectability. Thus, the observed differences in detection significance values across the instruments are justified by these architectural distinctions. Given the accordance between our simulations and real-time observations, it is anticipated that the ELT will surpass other ground-based observatories, paving the way for a new era in atmospheric studies with heightened sensitivity for detecting molecular signatures in exoplanet atmospheres. With a larger diameter of 39.3 meters and a resolution of 100000, ELT can probe molecules that are hard to observe using other instruments and disentangle molecular features with better precision.

#### 4. CONCLUSIONS

HJs and UHJs present us with a unique opportunity to characterize their atmospheres and determine the molecular abundances of O- and C-bearing species (Guillot et al. 2022), offering insights into the exotic chemical processes taking place within their atmospheres. The primary objective of this work was to investigate the atmospheres of WASP-77 A b (HJ) and WASP-76 b (UHJ) using three high-resolution ground-based spectrographs (GIANO-B, CARMENES, ANDES) and conduct a complementary analysis to assess the detectability of different molecular bands. Among all instruments, ANDES demonstrated significantly better precision in detecting molecular bands, thanks to its larger collecting area and higher instrumental resolution. The alignment between our simulation analyses and actual observations for both planets underscores the significance of utilizing the ELT. With its advanced capabilities, ELT holds the promise of significantly enhancing the ability to probe molecules within exoplanet atmospheres with better sensitivity, further advancing our understanding of these distant worlds.

Based on the diverse wavelength coverage and distinct instrumental parameters, spectrographs possess a sweet spot where they excel in detecting particular molecules with en-

hanced significance. Employing the cross-correlation spectroscopy method, we anticipate the detection of various molecules, including OH ( $1.15 \mu\text{m}$ : CARMENES, ANDES;  $1.60 \mu\text{m}$ : GIANO-B, CARMENES, ANDES),  $\text{H}_2\text{O}$  ( $0.90, 1.00 \mu\text{m}$ : GIANO-B, CARMENES, ANDES;  $0.94 \mu\text{m}$ : CARMENES, ANDES;  $1.10 \mu\text{m}$ : GIANO-B, ANDES),  $\text{CH}_4$  ( $1.00, 1.60 \mu\text{m}$ : ANDES), CO ( $1.55 \mu\text{m}$ : GIANO-B, ANDES), HCN ( $0.80 \mu\text{m}$ : CARMENES, ANDES),  $\text{NH}_3$  ( $1.00 \mu\text{m}$ : ANDES), and  $\text{H}_2\text{S}$  ( $1.60 \mu\text{m}$ : GIANO-B, ANDES) for WASP-76 b. This indeed encompasses molecular detection from single transit to a maximum of 3 transits for the planet (see Table 3). ANDES surpasses CARMENES and GIANO-B in terms of the instrumental capability for detecting most of the molecular bands with a single transit. More transits are usually favorable for detecting the molecules (e.g. OH, CO, and  $\text{H}_2\text{S}$ ) using GIANO-B and CARMENES spectrographs.

For WASP-77 A b, we have identified the presence of OH ( $1.15, 1.60 \mu\text{m}$ : ANDES),  $\text{H}_2\text{O}$  ( $0.90, 1.00 \mu\text{m}$ : GIANO-B, CARMENES, ANDES;  $0.94 \mu\text{m}$ : CARMENES, ANDES;  $1.10 \mu\text{m}$ : GIANO-B, ANDES), CO ( $1.55 \mu\text{m}$ : ANDES),  $\text{NH}_3$  ( $1.00 \mu\text{m}$ : ANDES) and  $\text{H}_2\text{S}$  ( $1.60 \mu\text{m}$ : ANDES). For both planets, we have reached a  $\sigma_{\text{det}} > 2$  for above mentioned molecular bands for different numbers of transits (see Tables 3 and 4). The spectral bands of  $\text{H}_2\text{O}$ , CO, OH,  $\text{NH}_3$ , and  $\text{H}_2\text{S}$  are sufficiently robust for WASP-76 b, enabling their detection with a  $\sigma_{\text{det}} > 3$  within 3 transits. Conversely, the signals are a little fainter for WASP-77 A b except  $\text{H}_2\text{O}$ . This prioritizes the need for more transits to significantly detect CO, OH,  $\text{NH}_3$ , and  $\text{H}_2\text{S}$  in the atmosphere of WASP-77 A b.

By examining the interlinked chemical network and molecular conversion pathways, we have developed a detailed understanding of the atmospheric chemistry on both planets. It is noteworthy that, aside from photolysis, OH can be formed through alternative reaction mechanisms from water. Additionally, within the photosphere, the rise in the OH mixing ratio is related to the depletion of  $\text{H}_2\text{O}$  and  $\text{NH}_3$ . Our efforts to identify HCN signatures in the atmosphere of WASP-76 b were inconclusive due to the extremely low VMR in our 1-D models. Nevertheless, we highlight the significance of nitrogen chemistry, particularly in the cooler night side of the planet (Sánchez-López et al. 2022). The non-detection of  $\text{CO}_2$  in the atmosphere of WASP-77 A b is consistent with recent JWST observations (August et al. 2023). The detection of  $\text{H}_2\text{S}$ , particularly on WASP-76 b, as the only sulfur-bearing molecular entity, serves as motivation for emphasizing the significance of sulfur chemistry within the atmospheres of irradiated gas giants.

## ACKNOWLEDGEMENTS

L.M. acknowledges financial support from DAE and DST-SERB research grants (SRG/2021/002116 and MTR/2021/000864) of the Government of India. D.D. also acknowledges financial support from the DST-SERB research grant SRG/2021/002116, which supported this work.

L.M. thanks Dr. Paul Mollière of MPIA Heidelberg, Germany, for providing access to petitCODE and for actively participating in discussions regarding its use and applications. We would like to thank the anonymous referee for constructive comments that helped improve the manuscript.

## REFERENCES

- Ackerman, A. S., & Marley, M. S. 2001, *The Astrophysical Journal*, 556, 872
- Alonso-Floriano, F. J., Sánchez-López, A., Snellen, I. A., et al. 2019, *Astronomy & Astrophysics*, 621, A74
- Arcangeli, J., Désert, J.-M., Line, M. R., et al. 2018, *The Astrophysical Journal Letters*, 855, L30
- August, P. C., Bean, J. L., Zhang, M., et al. 2023, arXiv preprint arXiv:2305.07753
- Bell, T. J., & Cowan, N. B. 2018, *The Astrophysical Journal Letters*, 857, L20
- Birkby, J., De Kok, R., Brogi, M., et al. 2013a, *Monthly Notices of the Royal Astronomical Society: Letters*, 436, L35
- Birkby, J., de Kok, R., Brogi, M., et al. 2013b, L35
- Birkby, J. L. 2018, arXiv preprint arXiv:1806.04617
- Borsato, N., Hoeijmakers, H., Cont, D., et al. 2024
- Brogi, M., De Kok, R., Albrecht, S., et al. 2016, *The Astrophysical Journal*, 817, 106
- Brogi, M., Giacobbe, P., Guilluy, G., et al. 2018, *Astronomy & Astrophysics*, 615, A16
- Brogi, M., & Line, M. R. 2019, *The Astronomical Journal*, 157, 114
- Brogi, M., Snellen, I. A., De Kok, R. J., et al. 2012, *Nature*, 486, 502
- Cabot, S. H., Madhusudhan, N., Hawker, G. A., & Gandhi, S. 2019, *Monthly Notices of the Royal Astronomical Society*, 482, 4422
- Carleo, I., Giacobbe, P., Guilluy, G., et al. 2022, *The Astronomical Journal*, 164, 101
- Casasayas-Barris, N., Pallé, E., Yan, F., et al. 2019, *Astronomy & Astrophysics*, 628, A9
- Changeat, Q., Edwards, B., Al-Refaie, A. F., et al. 2022, *The Astrophysical Journal Supplement Series*, 260, 3
- Chubb, K. L., Rocchetto, M., Yurchenko, S. N., et al. 2021, *Astronomy & Astrophysics*, 646, A21
- Cortés-Zuleta, P., Rojo, P., Wang, S., et al. 2020, *Astronomy & Astrophysics*, 636, A98
- Crossfield, I. J. 2015, *Publications of the Astronomical Society of the Pacific*, 127, 941
- Currie, M. H., Meadows, V. S., & Rasmussen, K. C. 2023, *The Planetary Science Journal*, 4, 83
- Dash, S., Majumdar, L., Willacy, K., et al. 2022, *The Astrophysical Journal*, 932, 20, doi: [10.3847/1538-4357/ac67f0](https://doi.org/10.3847/1538-4357/ac67f0)
- Di Marcantonio, P., Zanutta, A., Marconi, A., et al. 2022, in *Modeling, Systems Engineering, and Project Management for Astronomy X*, Vol. 12187, SPIE, 1218702
- Dijkstra, E. W. 2022, in *Edsger Wybe Dijkstra: His Life, Work, and Legacy*, 287–290
- Edwards, B., & Changeat, Q. 2024, *The Astrophysical Journal Letters*, 962, L30
- Edwards, B., Changeat, Q., Baeyens, R., et al. 2020, *The Astronomical Journal*, 160, 8, doi: [10.3847/1538-3881/ab9225](https://doi.org/10.3847/1538-3881/ab9225)
- Fortney, J. J., Lodders, K., Marley, M. S., & Freedman, R. S. 2008, *The Astrophysical Journal*, 678, 1419
- Giacobbe, P., Brogi, M., Gandhi, S., et al. 2021, *Nature*, 592, 205
- Guillot, T., Fletcher, L. N., Helled, R., et al. 2022, arXiv preprint arXiv:2205.04100
- Guilluy, G., Sozzetti, A., Brogi, M., et al. 2019, *Astronomy & Astrophysics*, 625, A107
- Hawker, G. A., Madhusudhan, N., Cabot, S. H., & Gandhi, S. 2018, *The Astrophysical Journal Letters*, 863, L11
- Hoch, K. K., Konopacky, Q. M., Theissen, C. A., et al. 2023, *The Astronomical Journal*, 166, 85
- Hoeijmakers, H. J., Ehrenreich, D., Kitzmann, D., et al. 2019, *Astronomy & Astrophysics*, 627, A165
- Hoeijmakers, H. J., Seidel, J. V., Pino, L., et al. 2020, *Astronomy & Astrophysics*, 641, A123
- Ivshina, E. S., & Winn, J. N. 2022, *The Astrophysical Journal Supplement Series*, 259, 62
- Landman, R., Sánchez-López, A., Mollière, P., et al. 2021, *Astronomy & Astrophysics*, 656, A119
- Line, M. R., Stevenson, K. B., Bean, J., et al. 2016, *The Astronomical Journal*, 152, 203
- Line, M. R., Brogi, M., Bean, J. L., et al. 2021, *Nature*, 598, 580
- Madhusudhan, N. 2012, *The Astrophysical Journal*, 758, 36
- Madhusudhan, N., & Seager, S. 2010, *The Astrophysical Journal*, 725, 261
- Maxted, P., Anderson, D., Cameron, A. C., et al. 2012, *Publications of the Astronomical Society of the Pacific*, 125, 48
- Molaverdikhani, K., Henning, T., & Mollière, P. 2019, *The Astrophysical Journal*, 873, 32
- Mollière, P., Wardenier, J. P., van Boekel, R., et al. 2019, *A&A*, 627, A67, doi: [10.1051/0004-6361/201935470](https://doi.org/10.1051/0004-6361/201935470)



- Mollière, Stolker, T., Lacour, S., et al. 2020, *A&A*, 640, A131, doi: [10.1051/0004-6361/202038325](https://doi.org/10.1051/0004-6361/202038325)
- Mollière, P., van Boekel, R., Dullemond, C., Henning, T., & Mordasini, C. 2015, *The Astrophysical Journal*, 813, 47
- Mollière, P. M. 2017, PhD thesis
- Ng, K.-C. 1974, *The Journal of Chemical Physics*, 61, 2680
- Noll, S., Kausch, W., Barden, M., et al. 2012, *Astronomy & Astrophysics*, 543, A92
- Nugroho, S. K., Kawahara, H., Gibson, N. P., et al. 2021, *The Astrophysical Journal Letters*, 910, L9
- Oliva, E., Origlia, L., Baffa, C., et al. 2006, in *Ground-based and Airborne Instrumentation for Astronomy*, Vol. 6269, SPIE, 431–440
- Oliva, E., Origlia, L., Maiolino, R., et al. 2012, in *Ground-based and Airborne Instrumentation for Astronomy IV*, Vol. 8446, SPIE, 1307–1315
- Olson, G. L., Auer, L., & Buchler, J. R. 1986, *Journal of Quantitative Spectroscopy and Radiative Transfer*, 35, 431
- Parmentier, V., Line, M. R., Bean, J. L., et al. 2018, *Astronomy & Astrophysics*, 617, A110
- Prinot, B., Hoeijmakers, H., Morris, B., et al. 2024, arXiv preprint arXiv:2403.08863
- Quirrenbach, A., Amado, P., Caballero, J., et al. 2014, in *Ground-based and Airborne Instrumentation for Astronomy V*, Vol. 9147, SPIE, 531–542
- Quirrenbach, A., Amado, P. J., Ribas, I., et al. 2018, in *Ground-based and Airborne Instrumentation for Astronomy VII*, Vol. 10702, SPIE, 246–263
- Redfield, S., Endl, M., Cochran, W. D., & Koesterke, L. 2008, *The Astrophysical Journal*, 673, L87
- Rothman, L. S., Gordon, I., Barber, R., et al. 2010, *Journal of Quantitative Spectroscopy and Radiative Transfer*, 111, 2139
- Sánchez-López, A., Landman, R., Mollière, P., et al. 2022, *Astronomy & Astrophysics*, 661, A78
- Sánchez-López, A., Alonso-Floriano, F. J., López-Puertas, M., et al. 2019, *Astronomy & Astrophysics*, 630, A53
- Sánchez-López, A., López-Puertas, M., Snellen, I., et al. 2020, *A&A*, 643, A24
- Seifert, W., Xu, W., Stahl, O., et al. 2016, in *Ground-based and Airborne Instrumentation for Astronomy VI*, Vol. 9908, SPIE, 1855–1867
- Smith, P. C., Line, M. R., Bean, J. L., et al. 2024, *The Astronomical Journal*, 167, 110
- Snellen, I., Albrecht, S., De Mooij, E., & Le Poole, R. 2008, *Astronomy & Astrophysics*, 487, 357
- Snellen, I. A., De Kok, R. J., De Mooij, E. J., & Albrecht, S. 2010, *Nature*, 465, 1049
- Southworth, J., Wheatley, P. J., & Sams, G. 2007, *Monthly Notices of the Royal Astronomical Society: Letters*, 379, L11
- Stock, J. W., Kitzmann, D., Patzer, A. B. C., & Sedlmayr, E. 2018, *Monthly Notices of the Royal Astronomical Society*, 479, 865
- Taberner, H., Osorio, M. Z., Allart, R., et al. 2021, *Astronomy & Astrophysics*, 646, A158
- Tsai, S.-M., Kitzmann, D., Lyons, J. R., et al. 2018, *The Astrophysical Journal*, 862, 31, doi: [10.3847/1538-4357/aac834](https://doi.org/10.3847/1538-4357/aac834)
- Tsai, S.-M., Lyons, J. R., Grosheintz, L., et al. 2017, *The Astrophysical Journal Supplement Series*, 228, 20, doi: [10.3847/1538-4365/228/2/20](https://doi.org/10.3847/1538-4365/228/2/20)
- Tsai, S.-M., Malik, M., Kitzmann, D., et al. 2021, *The Astrophysical Journal*, 923, 264, doi: [10.3847/1538-4357/ac29bc](https://doi.org/10.3847/1538-4357/ac29bc)
- West, R. G., Hellier, C., Almenara, J.-M., et al. 2016, *Astronomy & Astrophysics*, 585, A126
- Woitke, P., Helling, C., Hunter, G., et al. 2018, *Astronomy & Astrophysics*, 614, A1
- Wright, J., Marcy, G., Howard, A., et al. 2012, *The Astrophysical Journal*, 753, 160
- Wytenbach, A., Ehrenreich, D., Lovis, C., Udry, S., & Pepe, F. 2015, *Astronomy & Astrophysics*, 577, A62

## APPENDIX

## A. REACTION PROFILE DIAGRAMS FOR MOLECULAR INTERCONVERSIONS

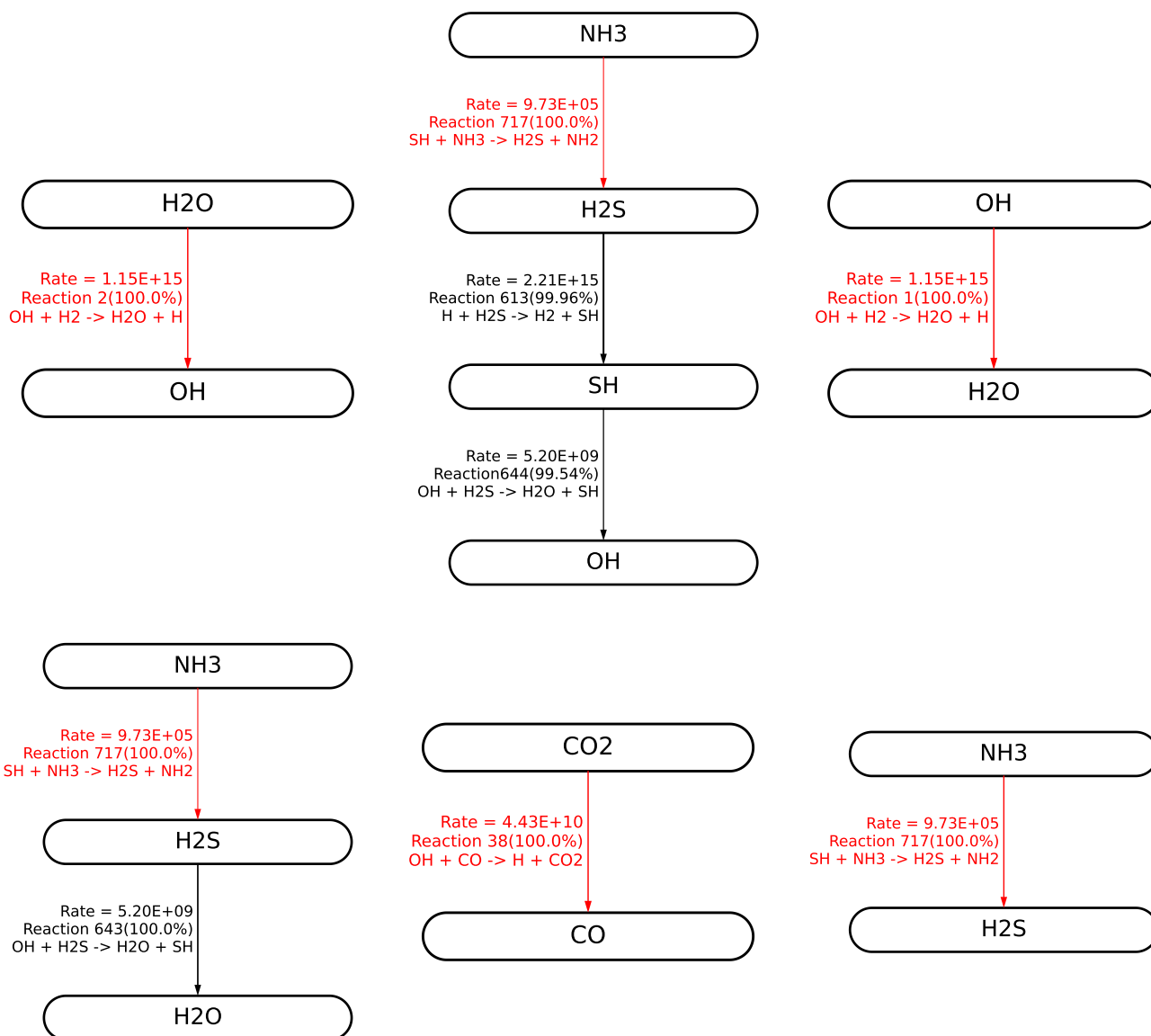


**Figure 11.** Shortest pathway analysis for molecular conversion using Dijkstra's algorithm at 0.01 bar. The conversion networks are shown based on Figure 6 for the atmosphere of WASP-77 A b. The texts besides the arrows explain the reactions involved (*First row*: reaction rates in  $\text{cm}^{-1}\text{s}^{-1}$ , *Second row*: reaction number from the VULCAN network. The odd number is for the forward reaction and the even number is for the backward reaction. The contribution of that particular reaction to the interconversion has also been provided in brackets. *Third row*: reaction involved in the interconversion.) Thicker black lines represent faster reactions, while the red lines represent the slowest reaction, i.e. the rate-limiting step for the molecular conversion pathway.

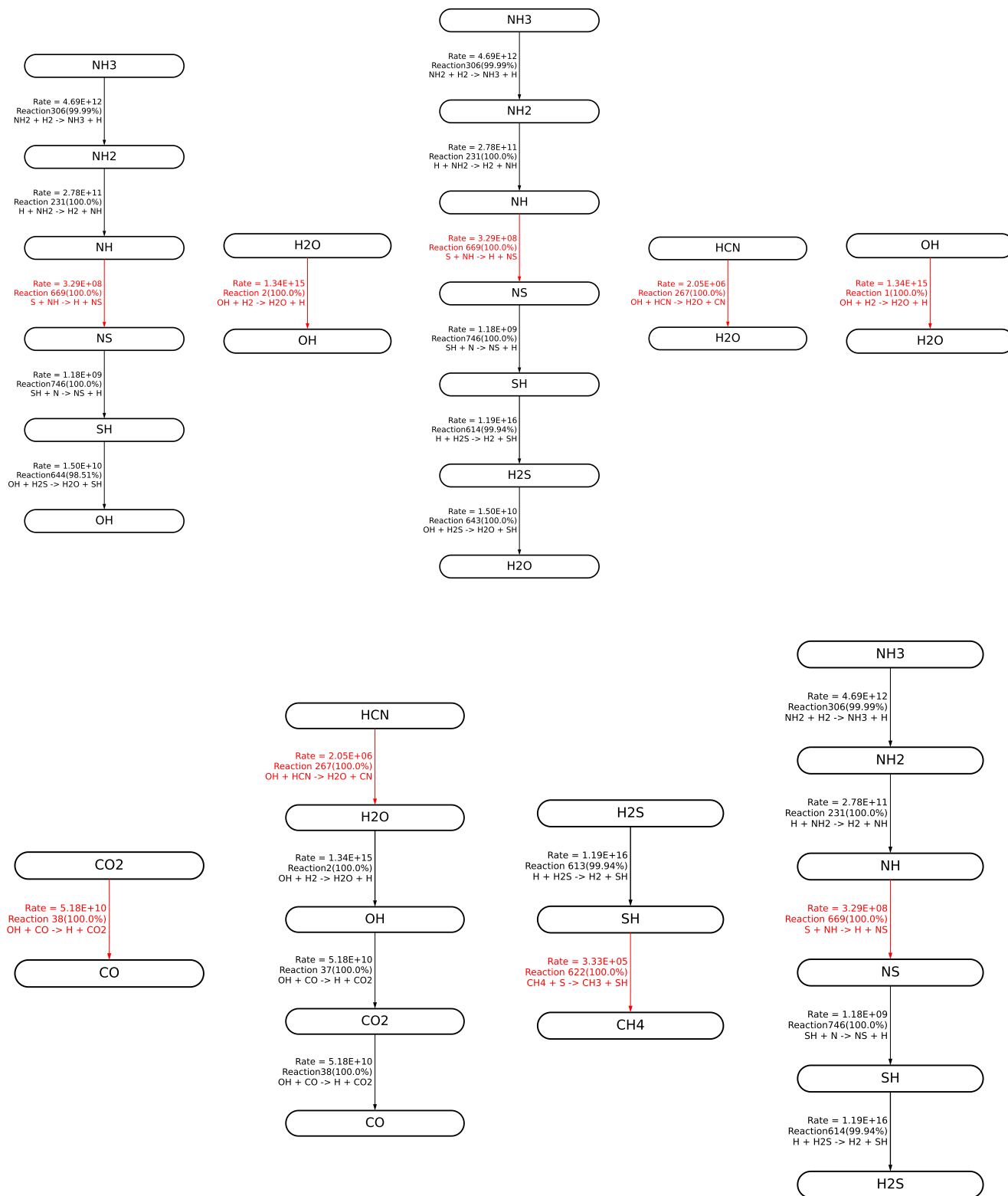


Figure 12. Same as Figure 11, but for the WASP-76 b molecular network in Figure 6.

## B. MOLECULAR BANDS OF WASP-76 B

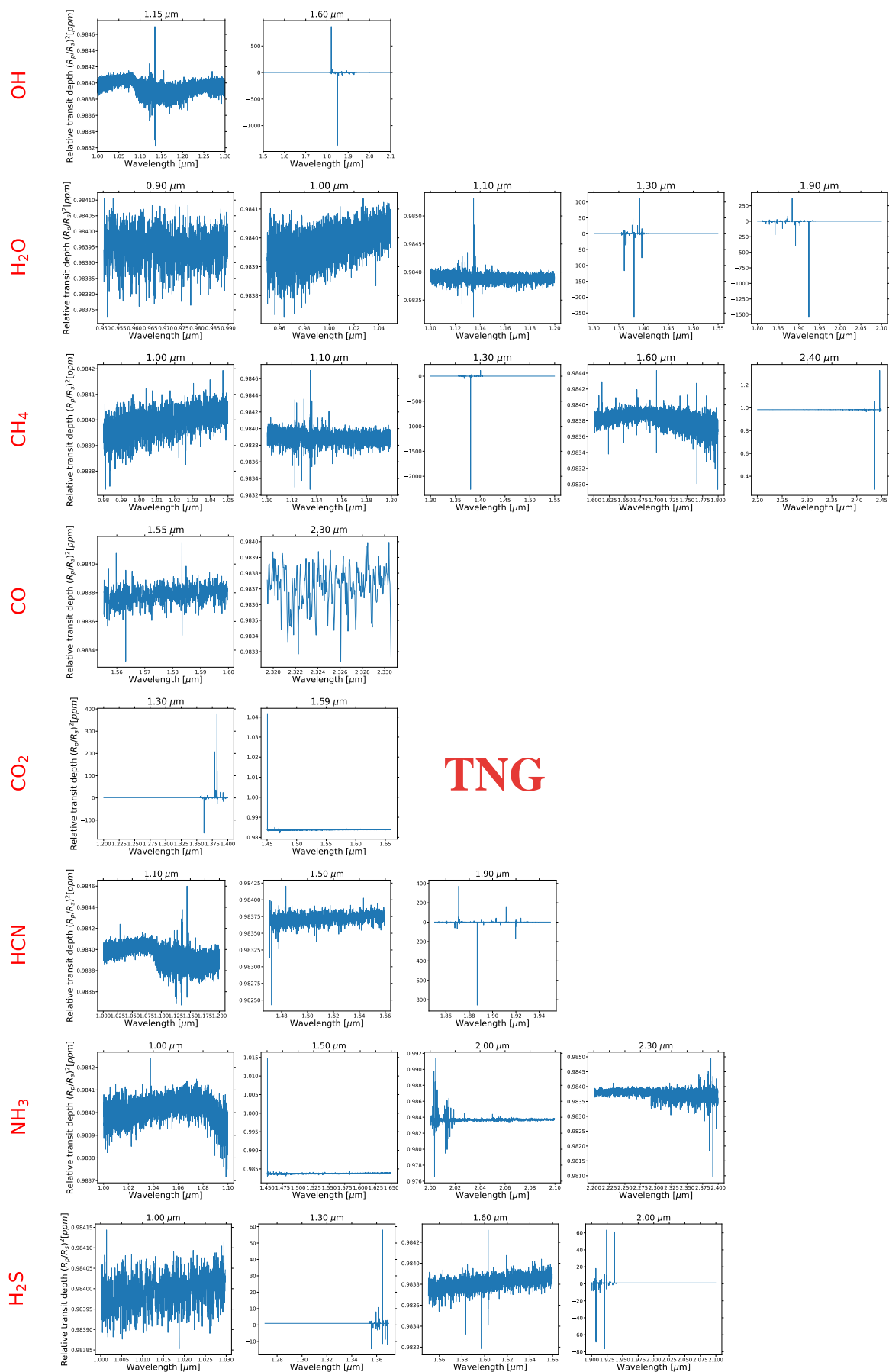


Figure 13. Continuum subtracted WASP-76 b molecular bands using high pass filters, calculated for 3 transits for TNG.

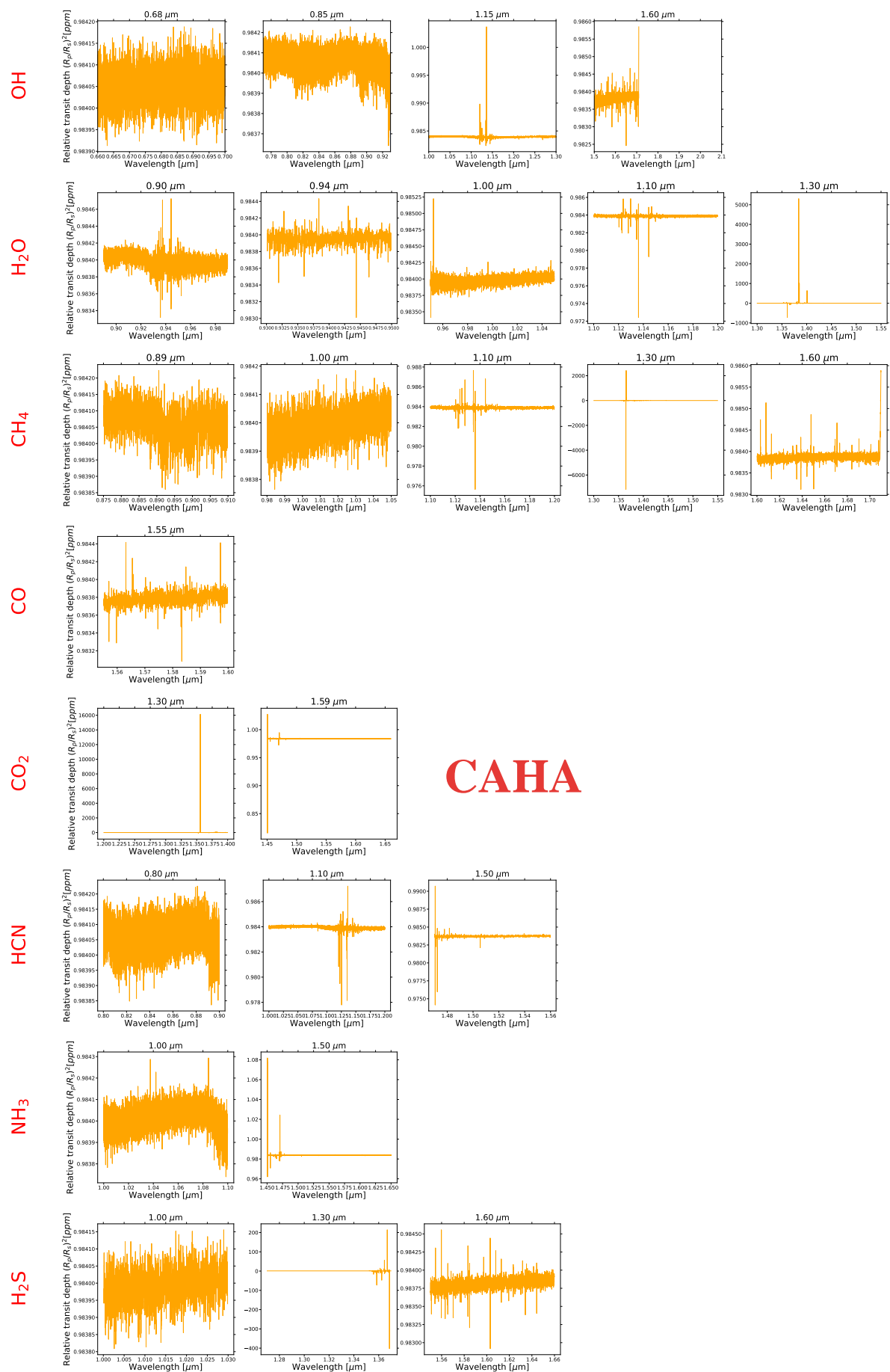


Figure 14. Same as Figure 13, but for CAHA.

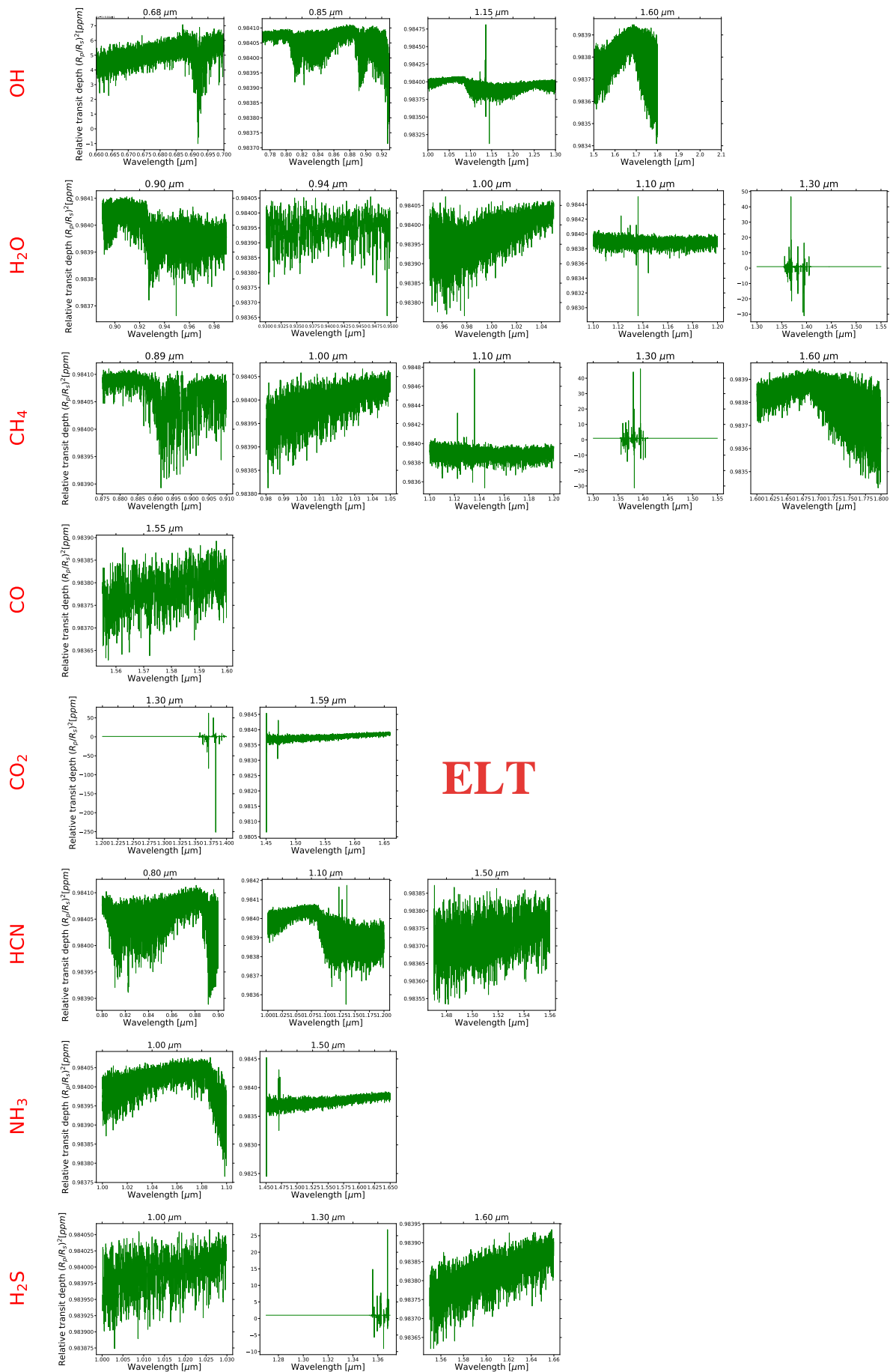


Figure 15. Same as Figure 13, but for ELT.

## C. MOLECULAR BANDS OF WASP-77 A B

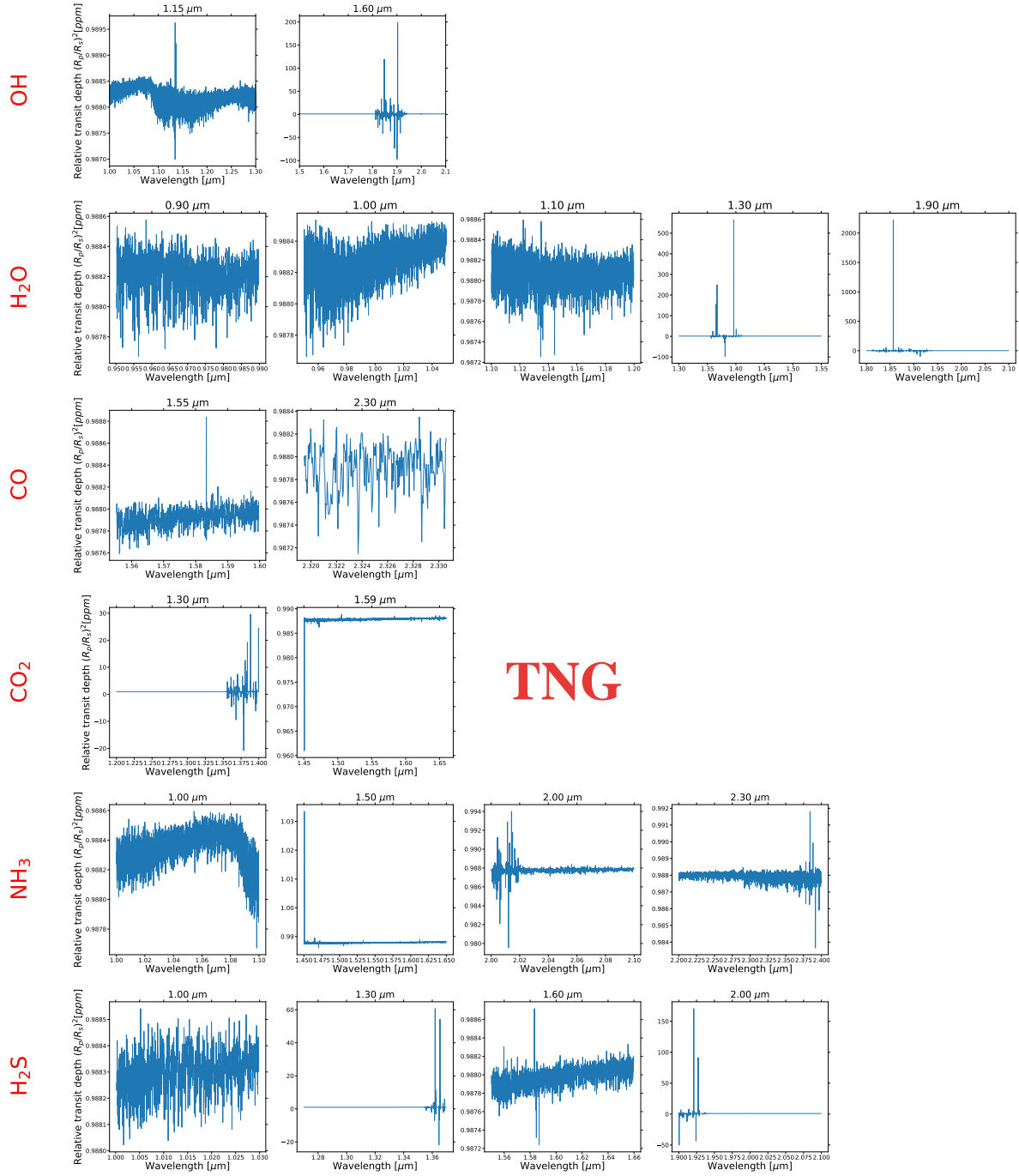


Figure 16. Continuum subtracted WASP-77 A b molecular bands using high pass filters, calculated for 3 transits for TNG.

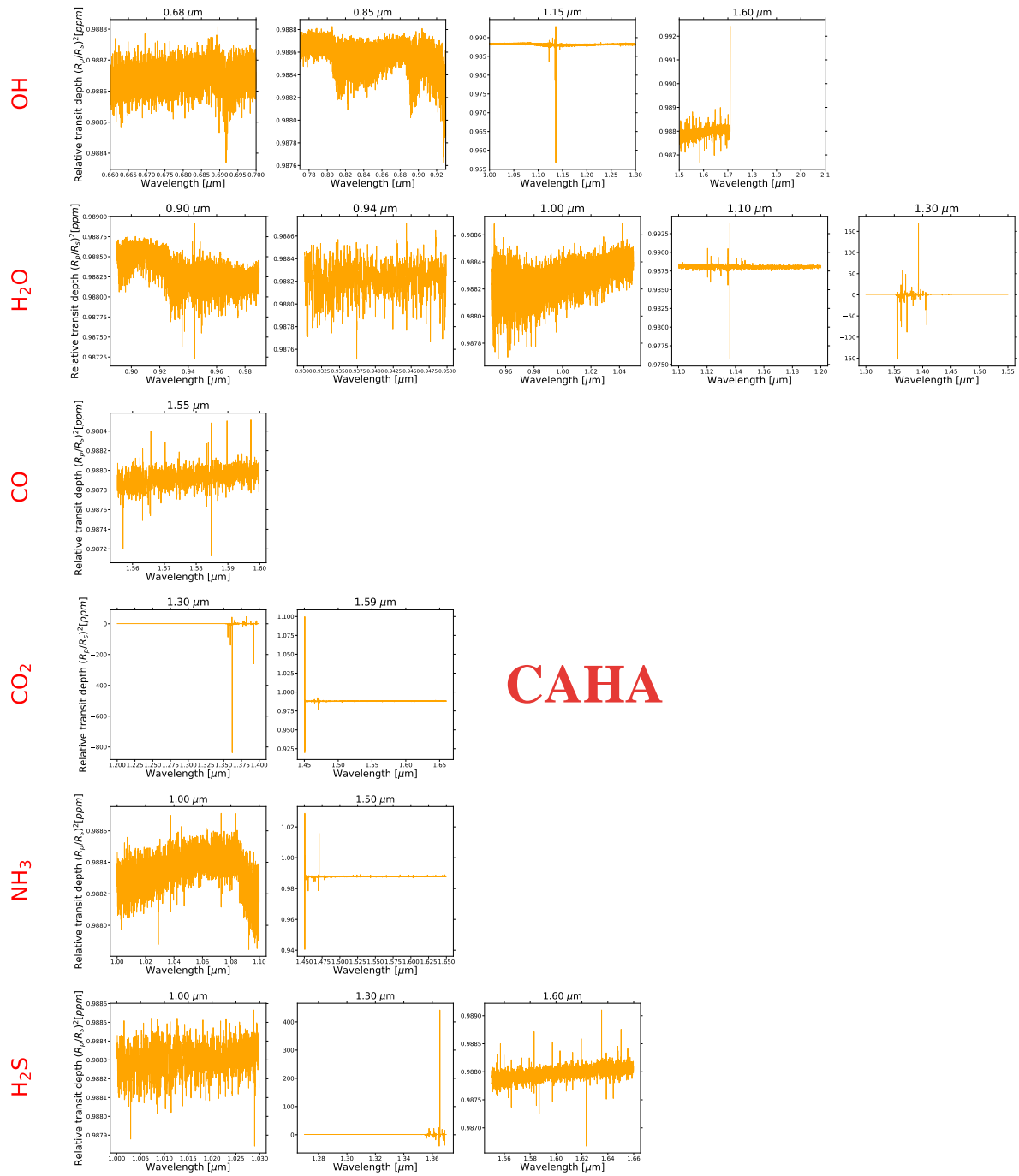


Figure 17. Same as Figure 16, but for CAHA.



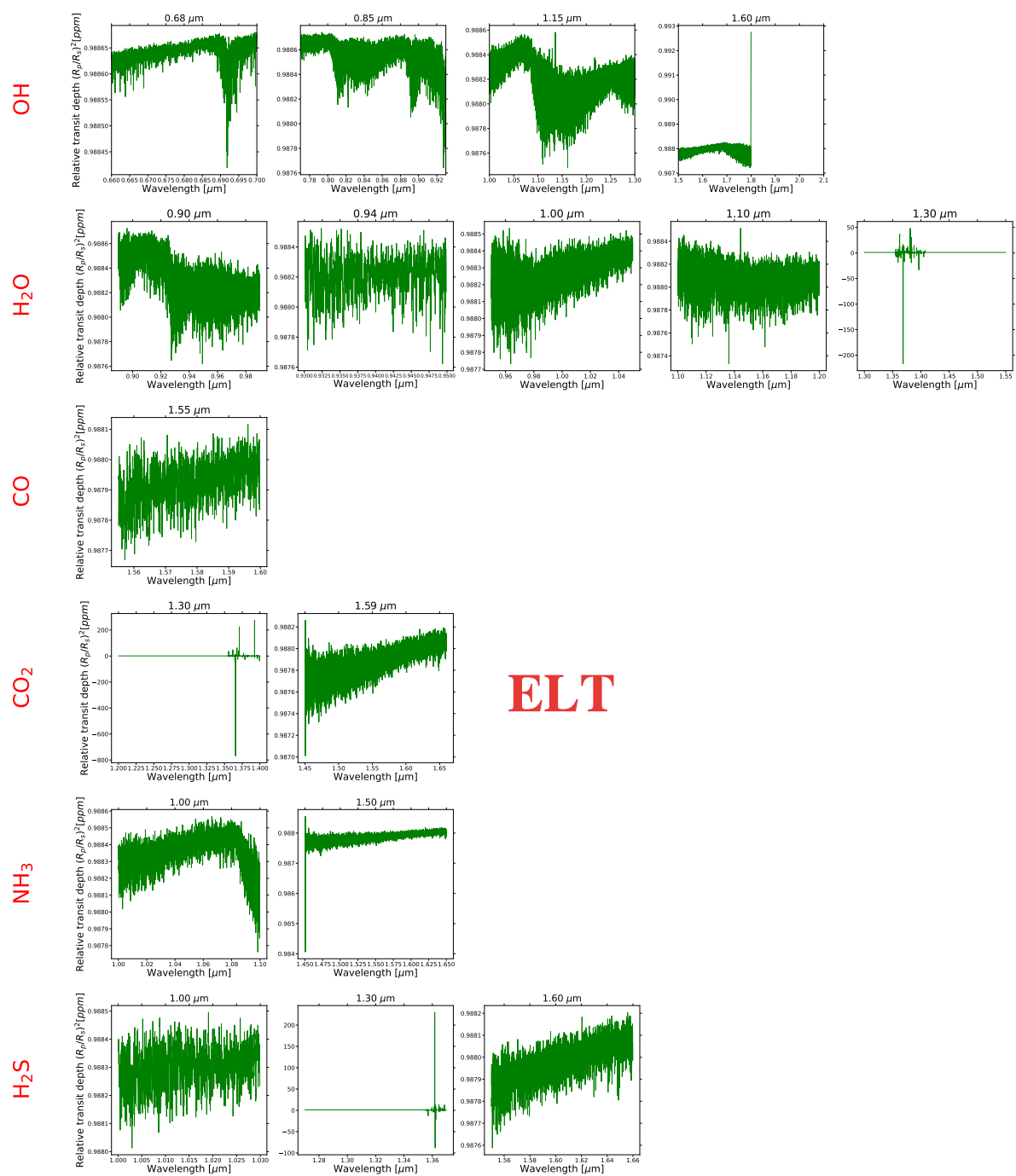


Figure 18. Same as Figure 16, but for ELT.